Near-wall PLIF Imaging of Formaldehyde in an HCCI Engine

by

Mark R. Schrewe

A thesis submitted in partial fulfillment
of the requirements for a degree of

Master of Science
(Mechanical Engineering)

at the

University of Wisconsin – Madison

2005

Thesis Approved

Advisor's Signature:_____

Advisor: Dr. Jaal B. Ghandhi

Associate Professor of Mechanical Engineering

Date:_____

Abstract

This project studied the characteristics of Homogeneous-Charge Compression Ignition (HCCI) combustion near the combustion chamber surfaces using Planar Laser-Induced Fluorescence (PLIF) of the intermediate combustion species formaldehyde. Motivation for this study is a more complete understanding of the thermochemistry associated with HCCI combustion in the thermal boundary layer near the chamber surfaces. Current multi-zone models are based on a mass distribution defined by predictions of the thermal boundary layers.

The engine used for this study was a single-cylinder optically accessible research engine, operating with a compression ratio of 9.4:1, at 600 RPM, with equivalence ratios ranging from 0.06 to 0.26 and an intake temperature of 90°C.

Formaldehyde fluorescence was excited by 355 nm light from a pulsed Nd:YAG laser using an innovative through-the-wall approach to avoid vignetting effects. Images were acquired with an intensified CCD camera and post-processing was performed to remove background signal interference. This technique allowed spatial resolution both across the field of view and into the combustion chamber with a resolution of 0.5 mm at the wall.

The data indicate the absence of a strong global thermal stratification effect near the chamber surfaces, with no preferred location for formaldehyde formation or consumption. In all cases, images show a small thermal boundary layer, counter to model predictions. Trends in formaldehyde concentration as a function of crank timing and equivalence ratio were consistent with the literature.

Acknowledgements

First and foremost I would like to thank my advisor, Professor Jaal Ghandhi, for the opportunity to work and study here at the ERC and for his abundant technical knowledge and advice. A lot of the extra time he put in when I needed help might have made him late for dinner more than once. Without his valuable guidance this project would be something far less, and I wouldn't have a degree.

I also had a lot of help from many of the other students here at the ERC. Sean Younger and I spent many hours just trying to figure out how everything worked and how to keep it working. Randy Herold was a huge help when it came to any work with the laser or emissions bench. Thanks to Nate Haugle and Victor Salazar for troubleshooting and just talking through problems and to Andy Bright for getting me started in the lab. Ryan Rudnitzki was a big help with initial laser setups and with keeping everything in perspective. Thank you, Laine Stager for providing your valuable support, encouragement, and proofreading skills. Thanks to everyone else unmentioned for being good friends.

I would also like to thank the staff at the ERC, especially Susie Strzelec in the office, for dealing with all of us and our desire to shirk paperwork. Many thanks also go to Ralph Braun in the basement, for providing his extensive knowledge of mechanical design, machining, and maintenance for the engine and equipment. Also, thanks to Josh Leach, for his underappreciated help in maintaining our computer system. Thank God these people exist.

Thanks to the Ford Motor Co. for providing the funding for this project through the University Research Program, in particular Tom Kenney and Jay Yang for their input.

Finally thanks to my parents, family, and friends. Your support and encouragement throughout my life has been a constant source of strength. Everything I have I owe to my parents who have instilled in me the confidence, inspiration, and morals that have put me where I am today and will lead me from here. For this, I will never be able to thank you enough.

Table of Contents

ABSTRACT ..... **i**

ACKNOWLEDGEMENTS ..... **ii**

TABLE OF CONTENTS ..... **iii**

LIST OF FIGURES ..... **v**

LIST OF TABLES ..... **viii**

1. INTRODUCTION **1**

1.1. MOTIVATION 1
1.2. OBJECTIVES 2
1.3. APPROACH 3
1.4. OUTLINE 3

2. LITERATURE REVIEW **5**

2.1. HCCI 5
2.1.1. Engine Operation *5*
2.1.2. Advantages and Disadvantages *10*
2.1.3. Modeling *13*
2.2. PLIF 17
2.2.1. Imaging Technique *17*
2.2.2. Laser Selection *18*
2.2.3. Camera *18*
2.2.4. Processing *19*
2.3. FORMALDEHYDE 20
2.3.1. Combustion Intermediate *20*
2.3.2. Fluorescing Properties *21*
2.4. NEAR-WALL MEASUREMENTS 21
2.4.1. Boundary Layer Basics *22*
2.4.2. Optics Geometry *23*

3. EXPERIMENTAL SETUP **24**

3.1. RESEARCH ENGINE 24
3.1.1. Base Engine *255*
3.1.2. Cylinder Head, Spacer Ring, Valve Timing *25*
3.1.3. Peripheral Engine Systems *27*
3.2. COMBUSTION DATA ACQUISITION 31
3.2.1. Cylinder Pressure Data *311*
3.2.2. Emissions Analyzer *33*
3.3. OPTICAL SETUP 34
3.3.1. Laser *34*
3.3.2. Beam Optics *35*
3.3.3. Camera *38*
3.3.4. Timing System *400*

4. OPTICAL OBSTACLES **42**

4.1. VIGNETTING 45
4.1.1. Vignetting Forms *46*
4.1.2. Vignetting Measurements *50*
4.1.3. Vignetting Conclusions *60*
4.2. FLARE 61
4.3. DEPTH OF FIELD 64

5. NEAR-WALL IMAGING OF FORMALDEHYDE IN AN HCCI ENGINE **68**

5.1. IMAGE ORIENTATION 68
5.2. SAMPLE DATA AND CORRECTION 70
5.3. SPATIAL RESOLUTION 75
5.3.1. Qualification *76*
5.3.2. Image Data *78*
5.4. TIMING SWEEP 79
5.4.1. Averaged Images *80*
5.4.2. Image Profiles *81*
5.4.3. Individual Cycle Data *82*
5.5. FUEL SWEEP 86
5.5.1. Averaged Images *87*
5.5.2. Intensity Profiles *88*
5.5.3. Individual Cycle Data *89*

6. SUMMARY AND CONCLUSIONS **91**

6.1. PROJECT SUMMARY 91
6.2. CONCLUSIONS 91
6.3. RECOMMENDATIONS FOR FUTURE WORK 92

BIBLIOGRAPHY **94**

APPENDIX A – PISTON RING DETAILS **97**

APPENDIX B – ENGINE COMPONENT DRAWINGS **98**

APPENDIX C – VALVE EVENTS **103**

APPENDIX D – INTAKE ORIFICE FLOW CALIBRATIONS **104**

APPENDIX E – FUEL INJECTOR FLOW CALIBRATIONS **105**

APPENDIX F – PRESSURE TRANSDUCER CALIBRATION **106**

List of Figures

FIGURE 2.1 TYPICAL PRESSURE AND CUMULATIVE HEAT RELEASE CURVES FOR AN HCCI ENGINE OPERATING WITH A FUEL SUCH AS N-HEPTANE THAT EXHIBITS TWO-STAGE HEAT RELEASE [25]. 6
FIGURE 2.2 IGNITION DELAY CONTOURS FOR F=0.10 (A) AND F=0.15 (B). MEASURED TEMPERATURE TRAJECTORY IS SHOWN WITH A SOLID BOLD LINE. CYLINDER PRESSURE AT THE TIME OF IGNITION IS SHOWN WITH A VERTICAL LINE [3]. 7
FIGURE 2.3 CYLINDER PRESSURE AND HEAT RELEASE RATE CURVES FOR A RANGE OF WATER INJECTION RATES. WATER INJECTED INCREASES IN THE INDICATED DIRECTION [4]. 8
FIGURE 2.4 CUMULATIVE HEAT RELEASE CURVES FOR VARIOUS EGR LEVELS IN AN HCCI ENGINE [5]. 9
FIGURE 2.5 CO (A) AND HC (B) EMISSIONS FOR VARIOUS FUELS IN AN HCCI ENGINE OVER A RANGE OF LOADS [6]. 12
FIGURE 2.6 MASS FRACTION AND CUMULATIVE MASS FRACTION AS A FUNCTION OF TEMPERATURE AND MASS DISTRIBUTION ACCORDING TO TEMPERATURE [12]..... 14
FIGURE 2.7 SINGLE-ZONE AND 10-ZONE MODEL AND EXPERIMENTAL PRESSURE TRACES FOR THREE LEVELS OF BOOST [12]. 15
FIGURE 2.8 DISTRIBUTION OF COMBUSTION QUALITY AT 6 BTDC FOR A RANGE OF EQUIVALENCE RATIOS AS PREDICTED BY 40-ZONE KIVA3V MODEL [26]. 16
FIGURE 2.9 EXPERIMENTAL CYLINDER WALL AND FLUID TEMPERATURE MEASUREMENTS NEAR THE COMBUSTION CHAMBER WALL. TEMPERATURES TAKEN AT TWO DIFFERENT CRANK TIMINGS [26]. 16
FIGURE 2.10 FORMALDEHYDE CONCENTRATIONS AS A FUNCTION OF CRANK POSITION FOR TWO EQUIVALENCE RATIOS [25]. 20
FIGURE 2.11 SPECTRALLY RESOLVED FORMALDEHYDE FLUORESCENCE SIGNAL [18]. 21
FIGURE 3.1 BOTTOM VIEW OF THE 2-VALVE PUSHROD CYLINDER HEAD [15]. 26
FIGURE 3.2 FUEL DELIVERY SYSTEM SCHEMATIC. 29
FIGURE 3.3 SAMPLE MOTORED AND FIRED PRESSURE TRACES FOR THE TRIPTANE ENGINE USING N-HEPTANE. 32
FIGURE 3.4 OPTICAL SETUP AND PATH OF LASER BEAM. 36
FIGURE 3.5 TRANSMITTANCE PLOT FOR UG-11 FILTER [30]. 37
FIGURE 3.6 TOP VIEW OF THE SPACER RING AND PISTON. PATH OF LASER INTO THE COMBUSTION CHAMBER THROUGH THE OPTICAL ACCESS WINDOW. 38
FIGURE 3.7 CCD PIXEL ARRAY DIAGRAM [17]. 39
FIGURE 3.8 DIAGRAM FOR TIMING SIGNAL PROCESSING. 41
FIGURE 4.1 DIAGRAM OF CONVENTIONAL ACCESS OF THE COMBUSTION CHAMBER IN AN OPTICAL ENGINE USING AN EXTENDED BOWDITCH PISTON [15]. 42
FIGURE 4.2 PISTON AS AN OBSTRUCTION TO STANDARD OPTICAL ACCESS FOR THE REGION OF INTEREST. 43
FIGURE 4.3 INITIAL METHOD OF OPTICAL ACCESS FOR NEAR-WALL MEASUREMENTS. 44

FIGURE 4.4 VIGNETTING SEEN IN A PHOTOGRAPH FOR TWO APERTURE SIZES. LEFT: *F*/1.4. RIGHT: *F*/5.6 [29]. 45
FIGURE 4.5 OPTICAL VIGNETTING AS A FUNCTION OF APERTURE SIZE. LEFT: *F*/1.4. RIGHT: *F*/5.6 [29]. 47
FIGURE 4.6 NATURAL VIGNETTING AS A FUNCTION OF A LIGHT SOURCE'S DISTANCE REMOVED FROM THE OPTICAL AXIS [29]. 48
FIGURE 4.7 DIAGRAM OF PROPOSED OBSTRUCTION VIGNETTING. 49
FIGURE 4.8 DIAGRAM OF DIMENSIONS FOR VIGNETTING DISTANCE PREDICTION EQUATION. .. 49
FIGURE 4.9 SAMPLE IMAGE FROM VIGNETTING EXPERIMENT. RIGHT: RAZOR BLADE. BOTTOM: 12.7 MM OBSTRUCTION. 52
FIGURE 4.10 IMAGE AND INTENSITY PROFILE, FOR INDICATED RANGE, OF A RAZOR BLADE AND 12.7 MM OBSTRUCTION PLACED IN FRONT OF A UNIFORM LIGHT SOURCE. IN THE PLOT, VIGNETTING EXISTS TO THE RIGHT OF THE VERTICAL DASHED LINE. 54
FIGURE 4.11 PLOTS OF RELATIVE INTENSITY VS. DISTANCE AWAY FROM THE OBSTRUCTION BOUNDARY FOR FOUR OBSTRUCTION DEPTHS (12.7, 38.1, 63.5, 88.9 MM). 55
FIGURE 4.12 RELATIVE INTENSITY AS A FUNCTION OF DISTANCE FROM THE OBSTRUCTION BOUNDARY NORMALIZED BY THE PREDICTED VIGNETTING DISTANCE FOR THE UNIFORM LIGHT SOURCE AND FOUR OBSTRUCTION DEPTHS (12.7, 38.1, 63.5, 88.9 MM). 55
FIGURE 4.13 IMAGE AND INTENSITY PROFILE, FOR INDICATED RANGE, OF A RAZOR BLADE AND 63.5 MM OBSTRUCTION PLACED IN FRONT OF A PLIF ILLUMINATED, DYE-FILLED CUVETTE LIGHT SOURCE. IN THE PLOT, VIGNETTING EXISTS TO THE RIGHT OF THE VERTICAL DASHED LINE. 56
FIGURE 4.14 PLOTS OF RELATIVE INTENSITY VS. DISTANCE AWAY FROM THE OBSTRUCTION BOUNDARY FOR FOUR OBSTRUCTION DEPTHS (12.7, 38.1, 63.5, 88.9 MM). 58
FIGURE 4.15 RELATIVE INTENSITY AS A FUNCTION OF DISTANCE FROM THE OBSTRUCTION BOUNDARY NORMALIZED BY THE PREDICTED VIGNETTING DISTANCE FOR THE PLIF ILLUMINATED LIGHT SOURCE AND FOUR OBSTRUCTION DEPTHS (12.7, 38.1, 63.5, 88.9 MM). 58
FIGURE 4.16 ENLARGED VIEW OF THE LASER SHEET PASSING THROUGH THE ACCESS WINDOW WITH RESULTING FLARE AND METHODS FOR REMOVING FLARE (OBSTRUCTION & FILTER). 62
FIGURE 4.17 TRANSMITTANCE PLOT FOR GG-400 HIGH PASS FILTER [30]. 63
FIGURE 4.18 TRANSMITTANCE PLOT FOR 505FD64-50S LOW PASS FILTER [31]. 63
FIGURE 4.19 DIAGRAM OF LASER SHEET ENTERING COMBUSTION CHAMBER THROUGH ACCESS WINDOW WITH DEPTH OF FIELD CONSIDERATIONS. 65
FIGURE 4.20 FLOW CHART OF CONSEQUENCES FOR INCIDENT ANGLE CALCULATIONS. 66
FIGURE 4.21 DIAGRAM OF METHOD FOR CALCULATING THE LASER SHEET INCIDENT ANGLE. 67
FIGURE 5.1 SAMPLE DATA IMAGES OF PLIF ILLUMINATED FORMALDEHYDE. 68
FIGURE 5.2 TOP VIEW OF ENGINE SPACER RING ASSEMBLY, PISTON, AND LASER PATH. 69
FIGURE 5.3 FRONT VIEW OF ENGINE SPACER RING ASSEMBLY, PISTON, AND LASER ILLUMINATED FIELD. 70
FIGURE 5.4 AVERAGED BACKGROUND (A) AND CORRECTED DATA (B) IMAGES FOR 8 MG OF FUEL PER CYCLE AT 10° BTDC. 71
FIGURE 5.5 PISTON FLARE VISIBLE IN AVERAGED BACKGROUND (A), INDIVIDUAL FIRED (B), AND AVERAGED CORRECTED (C) DATA IMAGES. 72

FIGURE 5.6 WINDOW FLARE VISIBLE IN AVERAGED BACKGROUND (A), INDIVIDUAL FIRED (B), AND AVERAGED CORRECTED (C) DATA IMAGES. 72
FIGURE 5.7 IMAGE OF THE RATIO OF DATA IMAGE INTENSITY TO BACKGROUND IMAGE INTENSITY AND INTENSITY PROFILE FOR THE LINE INDICATED ON THE IMAGE. 73
FIGURE 5.8 SAMPLE OF BACKGROUND IMAGES TAKEN AT 17° BTDC. VISIBLE IS PISTON AND WINDOW FLARE. 74
FIGURE 5.9 SAMPLE OF INDIVIDUAL FIRED IMAGES TAKEN AT 20° BTDC WITH 7 MG FUELING. 75
FIGURE 5.10 IMAGES OF BUCKY BADGER SHOWING RELATIVE FOCUS AT A RANGE OF DISTANCES FROM THE INNER WINDOW SURFACE. LEFT TO RIGHT: 1, 3, 6, 8 MM. 76
FIGURE 5.11 QUANTIFICATION OF SPATIAL RESOLUTION AT THE INNER WINDOW SURFACE. .. 77
FIGURE 5.12 IMAGES OF AVERAGED BACKGROUND (A), AVERAGED FIRED (B), AND TWO INDIVIDUAL FIRED CYCLES (C&D) WITH INDICATED HEIGHT OF INTENSITY PROFILE. 78
FIGURE 5.13 INTENSITY PROFILE FOR THE FOUR IMAGES IN FIGURE 5.12. 79
FIGURE 5.14 PRESSURE (MOTORED AND FIRED) AND HEAT RELEASE CURVES AT 8 MG FUELING FOR TIMING SWEEP DATA. VERTICAL LINES ARE IMAGE TIMINGS (23, 15, 10, 6, 5, AND 2° BTDC. 80
FIGURE 5.15 AVERAGE CORRECTED FIRED DATA IMAGES FOR THE TIMINGS INDICATED AT A FUELING RATE OF 8 MG/CYCLE. 81
FIGURE 5.16 AVERAGED INTENSITY PROFILES AT THE WINDOW SURFACE FOR THE TIMINGS INDICATED AT 8 MG/CYCLE FUELING. 82
FIGURE 5.17 RANDOM IMAGES FROM EACH IMAGE TIMING (INDICATED TOP). IMAGE INTENSITY IS SCALED TO SHOW DETAIL (RELATIVE SCALE INDICATED BOTTOM). 83
FIGURE 5.18 INTENSITY PROFILE FOR AVERAGE CORRECTED FIRED IMAGE AND TWO INDIVIDUAL CYCLE IMAGES FOR 8 MG/CYCLE FUELING, ACQUIRED AT 23° BTDC. 84
FIGURE 5.19 INTENSITY PROFILE FOR AVERAGE CORRECTED FIRED IMAGE AND TWO INDIVIDUAL CYCLE IMAGES FOR 8 MG/CYCLE FUELING, ACQUIRED AT 2° BTDC. 85
FIGURE 5.20 AVERAGE BACKGROUND (A) AND CORRECTED FIRED (B) DATA IMAGES FOR FUELING OF 8 MG/CYCLE TAKEN AT TDC. 85
FIGURE 5.21 PRESSURE AND HEAT RELEASE CURVES FOR FUELING RATES OF 2, 5, 7, AND 8 MG/CYCLE. VERTICAL LINES INDICATE IMAGE TIMINGS (10 AND 12° BTDC). 86
FIGURE 5.22 AVERAGE CORRECTED FIRED DATA IMAGES FOR THE FUELING RATES INDICATED AT TIMINGS OF 10 AND 12° BTDC. 87
FIGURE 5.23 FORMALDEHYDE SIGNAL PRESENT AT 20° ATDC FOR A FUELING RATE OF 2 MG/CYCLE. 87
FIGURE 5.24 AVERAGED INTENSITY PROFILES AT THE WINDOW SURFACE FOR THE FUELING RATES INDICATED AT 10 AND 12° BTDC. 88
FIGURE 5.25 RANDOM IMAGES FROM EACH IMAGE FUELING (INDICATED TOP). IMAGE INTENSITY IS SCALED TO SHOW DETAIL (RELATIVE SCALE INDICATED BOTTOM). 90
FIGURE 5.26 INTENSITY PROFILE FOR AVERAGE CORRECTED FIRED IMAGE AND TWO INDIVIDUAL CYCLE IMAGES FOR 2 MG/CYCLE FUELING, ACQUIRED AT 10° BTDC. 90

List of Tables

TABLE 3.1 FIXED DIMENSIONS AND TIMINGS FOR GM-TRIPTANE ENGINE. VALVE TIMINGS ARE MEASURED FROM TDC COMPRESSION..... 24
TABLE 3.2 SERIAL NUMBERS FOR SPECIES ANALYZERS ON HORIBA EMISSIONS BENCH..... 34
TABLE 4.1 VIGNETTING CALCULATION RESULTS SUMMARY FOR OBSTRUCTION DEPTHS GENERATED BY 0.5, 1.5, 2.5, AND 3.5 INCH GAUGE BLOCKS IN FRONT OF A PLIF-ILLUMINATED DYE. 59

1. Introduction

1.1. Motivation

Homogeneous-Charge Compression-Ignition (HCCI) combustion has the potential for extremely efficient and clean operation. Characterized by thermal efficiencies equal to or greater than that of diesel engines, and promises of low emissions due to a well mixed intake charge and cool combustion temperatures, HCCI combustion has been the subject of a great deal of research over the past two decades.

Currently HCCI combustion is in the research stage of development. Major hurdles including control, knock, etc. still prevent HCCI from production use. In order to advance the technology, research is focused on studying the characteristics and performance of HCCI combustion. A better understanding of this combustion process will hopefully suggest future paths for the development of techniques to overcome the present obstacles.

One area important to understanding the overall combustion process is the effect of quenching near the walls of the combustion chamber. Heat transfer from the gases to the cooler chamber walls causes the reaction to quench, resulting in unburned-hydrocarbons (uHC). A large portion of the uHC emissions problems for HCCI combustion come from the near wall quenching. This is especially a problem at light load where the burned gas temperatures are low.

To study the details of the combustion near the cylinder walls, formaldehyde was used as a combustion indicator. Formaldehyde is formed during the first stage of ignition and consumed during the second stage of ignition for fuels like n-heptane that exhibit cool-

flame chemistry. Measuring the relative amounts of formaldehyde present in the combustion chamber at various crank angles can give an indication as to how the combustion is progressing.

Near-wall combustion has to this point been relatively unexplored experimentally. Various computer models have been developed to predict HCCI combustion using computational fluid dynamics (CFD) and chemical kinetics, but a well-developed boundary layer model has yet to be universally implemented. Different methods for modeling boundary layer effects have been used, but very little experimental data exists to confirm their predictions.

This study will attempt to provide data on the characteristics of near-wall HCCI combustion to provide further insights into the HCCI combustion process, especially at light load. It will also, hopefully, give guidance for modeling the chemical kinetics occurring in the combustion chamber, especially near the cylinder surfaces.

1.2. Objectives

There are four objectives central to the undertaken research:

1. To obtain spatially and temporally resolved, two-dimensional images of the formaldehyde concentration near the combustion chamber surfaces.
2. To correlate the image data with engine performance such as cylinder pressure and heat release data for a range of equivalence ratios and at various timings.
3. To draw conclusions about the boundary layer effects in HCCI combustion that will further the understanding of the combustion process and aid in future development of combustion models.

4. To demonstrate the use of Planar Laser-Induced Fluorescence (PLIF) as a tool for in-cylinder combustion measurements.

1.3. Approach

The main diagnostic technique implemented in this study was Planar Laser-Induced Fluorescence (PLIF). Through the use of a high-speed Intensified Charge-Coupled Device (ICCD) camera and a pulsed Nd:YAG laser, images were taken through a window located in the clearance volume of the chamber. The third harmonic of the laser (λ = 355nm) was used to excite formaldehyde fluorescence in a two-dimensional field of the combustion chamber near the cylinder wall. Measurements were taken to spatially and temporally determine the concentration of formaldehyde in the illuminated field.

1.4. Outline

This thesis will be divided in to five subsequent chapters. Chapter 2 is a literature review of the current state of HCCI combustion technology including modeling methods, PLIF techniques and results, the use of formaldehyde as a combustion indicator, and the significance and results of near-wall measurements. Chapter 3 describes the experimental facility used for the study. It details the specifics of the research engine, the engine diagnostic equipment, and the optical and image acquisition systems. Chapter 4 discusses optical difficulties associated with this experiment. One difficulty, called vignetting, played a significant role in determining the approach used in this study. Chapter 5 will deal with the results of this study. Image data will be presented as well as an analysis of what was

discovered. Finally Chapter 6 will be a summary of the project with conclusions and recommendations for future work and methods.

2. Literature Review

2.1. HCCI

Homogeneous Charge Compression Ignition (HCCI) combustion occurs when a charge of premixed fuel and air is compressed until the auto-ignition point of the mixture is reached and the mixture spontaneously ignites. This combustion cycle attempts to take advantage of the best qualities of both the spark ignition (SI) and compression ignition cycles. Its premixed charge allows for complete combustion with low emissions similar to the spark ignition engine, and the homogeneous ignition and combustion gives efficiencies similar to those achieved in a diesel engine. HCCI combustion has one main characteristic that distinguishes it from the two commercially used engine cycles. There is no flame front propagation through the combustion chamber. Multiple points in the combustion chamber ignite simultaneously, resulting in a compression of the remaining fluid until it auto-ignites as well. When used in automotive engine applications, HCCI yields increased efficiencies and reduced emissions at low load operating conditions [1]. Auto-ignition is controlled by altering the fuel composition and/or the temperature history of the mixture through the intake and compression path [2].

2.1.1. Engine Operation

HCCI combustion has the advantageous characteristics of a spark ignition and diesel engine. In HCCI engines, fuel is injected upstream of the intake valve in order to achieve complete homogeneity by the time the intake charge enters the cylinder. This homogeneous

mixture enters the combustion chamber and is compressed until auto-ignition takes place. Ignition is dependent upon only mixture composition and temperature history. Ignition occurs at multiple points simultaneously because of the homogeneous nature of the fluid, and the combustion proceeds without an identifiable flame front. Typical heat release rate and pressure traces are shown in Figure 2.1 for n-heptane, which exhibits a two-stage ignition.

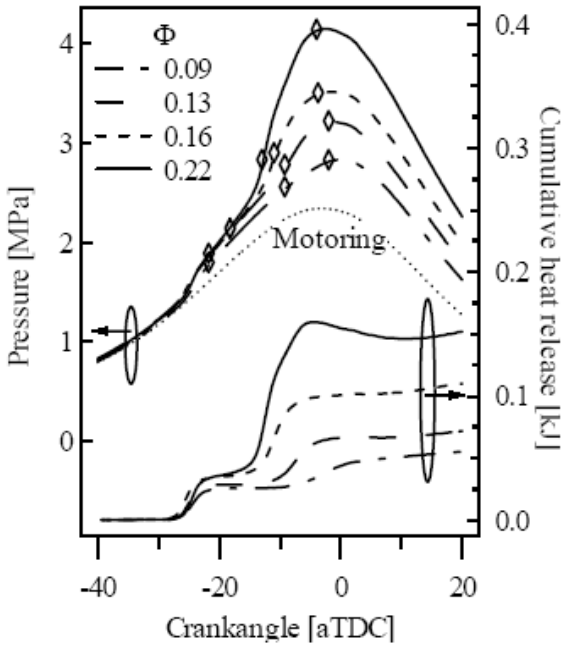

Figure 2.1 Typical pressure and cumulative heat release curves for an HCCI engine operating with a fuel such as n-heptane that exhibits two-stage heat release [25].

HCCI lacks hot spot or particle-induced ignition sources; combustion is dependent only on the chemical kinetics of the mixture and can be understood using global hydrocarbon kinetics. The two-stage heat release is the result of the negative temperature coefficient relationship between ignition delay and mixture temperature [2]. The first stage low level heat release is associated with low temperature chemical kinetics. These are dominated by chain propagation steps involving oxygen. This is followed by a heat release delay as a result of an

increase in ignition delay time at temperatures between 750 and 1000 K [3]. A plot of ignition delay is represented on a pressure-temperature plot in Figure 2.2. Second stage heat release follows, dominated by thermal decomposition of C-C bonds.

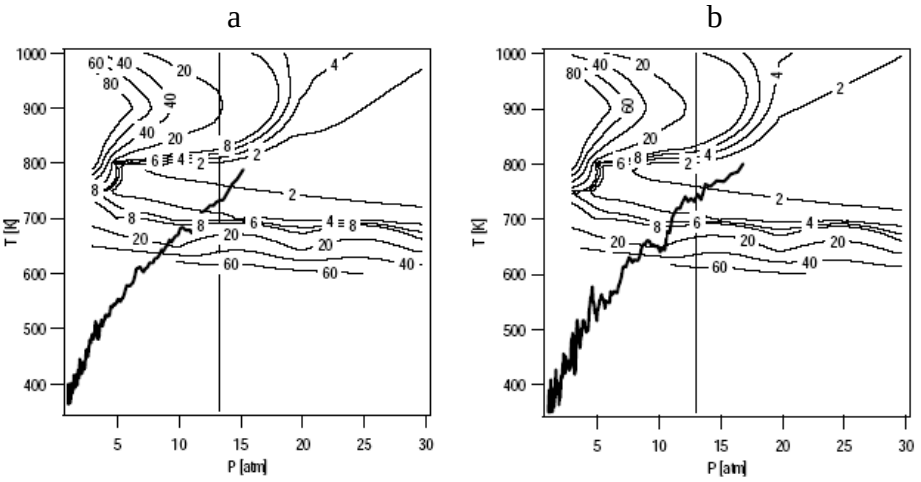

Figure 2.2 Ignition delay contours for Φ=0.10 (a) and Φ=0.15 (b). Measured temperature trajectory is shown with a solid bold line. Cylinder pressure at the time of ignition is shown with a vertical line [3].

In order to achieve significantly low heat release rates, HCCI is operated at lean equivalence ratios. HCCI operation is, therefore, limited to low load operation. Load control is achieved via the amount of fuel inducted into the cylinder (equivalence ratio) similar to that of a diesel engine.

Because of the nature of HCCI combustion, the time at which ignition takes place is very difficult to control; there is no direct control over ignition timing. Only indirectly can attempts be made to regulate the phasing of HCCI combustion [4]. As a result, transient control and higher equivalence/higher load operation is extremely difficult to predict given the sensitivity to other engine and powertrain parameters.

There are two main methods for controlling the auto-ignition that occurs in HCCI combustion. Determining the temperature history of the pre-mixed intake charge and regulating the chemical makeup of the charge can lead to some amount of control over the timing and intensity of the combustion process [2]. Within these two strategies there are several options that have been attempted. To alter the temperature history of the mixture, the easiest option for research purposes is to preheat the intake temperature. Increasing the intake temperature ensures combustion at lean operating conditions; however, penalties in the form of reduced volumetric efficiencies accompany higher intake temperatures due to the lower density of the mixture. Due to cost, energy, and size constraints, this is not viable for mobile applications [1]. Injecting water into the cylinder has also been used to delay ignition timing and slow the rate of heat release. Water injection was shown to delay combustion, extend combustion duration, and reduce heat release rates as the volume per cycle was increased. Figure 2.3 shows that an increase of water in the intake charge decreases peak pressures and slows heat release and ignition.

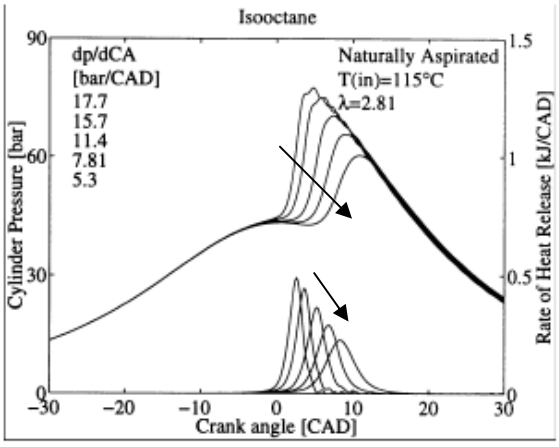

Figure 2.3 Cylinder pressure and heat release rate curves for a range of water injection rates. Water injected increases in the indicated direction [4].

This allows for higher load operation due to reduced peak pressures and lower pressure rise rates. Water addition is only successful for a very narrow engine load range. Penalties include an increase in quantities of unburned hydrocarbons and CO. NO_x emissions were reduced [4]. Varying the engine's compression ratio with variable valve timing (VVT) has also been employed.

Within the strategy of altering the chemical reactivity, the most popular idea is the use of Exhaust Gas Recirculation (EGR) to heat the mixture as well as cool the combustion reaction. Heating the intake charge strengthens combustion of the diluted mixture and therefore extends the operating range of HCCI combustion. Decreasing the reaction temperature or adiabatic flame temperature leads to the reduction of NO_x emissions which are formed at higher temperatures. It has been shown that the addition of EGR to the intake charge up to 69% by mass results in the delay of auto-ignition [5]. Figure 2.4 is a plot of heat release curves for various equivalence ratios and EGR fractions.

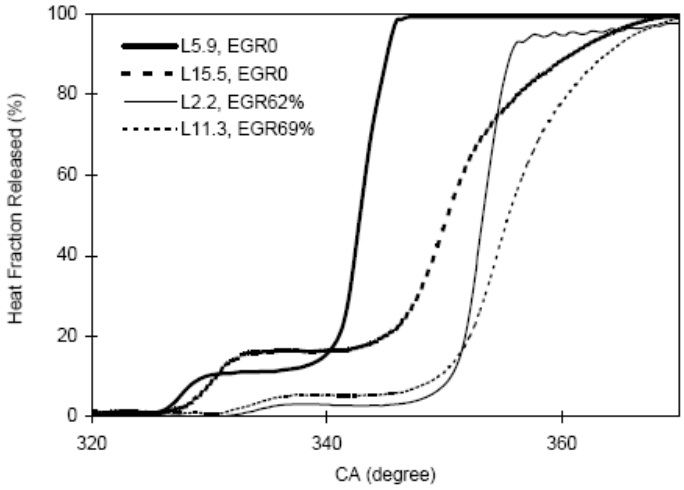

Figure 2.4 Cumulative heat release curves for various EGR levels in an HCCI engine [5].

2.1.2. Advantages and Disadvantages

HCCI combustion attempts to emulate the high efficiency of diesel engines while maintaining the low emissions of an SI engine. This is accomplished through the simultaneous multi-point ignition that results from mixture auto-ignition. This ignition process, however, also puts a load limit on the engine due to excessively rapid heat release. In addition, control becomes a significant issue with premixed auto-ignition.
Research at the Lund Institute of Technology [6,7] has shown that indicated thermal efficiencies approaching 50% can be achieved with HCCI combustion. Thermal efficiency is the relationship between the actual work done per cycle to the amount of fuel chemical energy released during combustion [8].

$$\eta_t = \frac{W_c}{H_R(T_A) - H_P(T_A)}$$

Combustion efficiencies are defined as the fraction of the fuel energy supplied to the cycle that is released in a chemical reaction [8]. In the same study, combustion efficiency was shown to exceed 90% [6].

$$\eta_c = \frac{H_R(T_A) - H_P(T_A)}{m_f * Q_{HV}}$$

Another factor for improving the efficiency of HCCI operation is that, like conventional diesel engines, the load is controlled by the mass of fuel delivered per cycle and not a throttling mechanism. The unrestricted air flow means higher pressure charges and lower pumping losses.

HCCI allows for a portion of the heat release to occur at low temperatures when using a two-stage combustion fuel such as n-heptane. This is advantageous since NO_x formation

increases with a rise in reaction temperature. Research in [2] and [9] has shown the presence of low temperature kinetics (below 1000 K) in two-stage combustion to be responsible for reduced NO_x emissions. Ignition in HCCI combustion occurs at temperatures around 1000 K. In contrast, conventional diesel engines exhibit minimum flame temperatures between 1900 and 2100 K, which is high enough to produce significantly higher amounts of NO_x. Below 0.01 g/kWh of NO_x was measured in HCCI combustion of various fuels [6]. As equivalence ratio is increased, NO_x formation also rises due to higher burning temperatures at equivalence ratios approaching 1.0.

Particulate matter, or soot formation, is also reduced with HCCI operation. Evidence shows a reduction in soot generation and formation is the result of the absence of a flame front or diffusion-limited combustion and stratified fuel-rich zones [1]. Soot forms in a typical diesel engine from the carbon in the diesel fuel. Formation occurs during combustion at temperatures between 1000 and 2800 K [8].

Not all HCCI emission results are improvements over standard diesel engines. Both carbon monoxide (CO) and unburned hydrocarbon (uHC) emissions have been found to be higher than what is typically found in compression ignition engines. High CO emissions are typically an indicator of incomplete combustion. Since loads on HCCI engines are usually very low, incomplete combustion and even misfires can occur at the lean limits. CO measurements in research on HCCI emissions ranged from 2 to 15 g/kWh with natural aspiration and tended to decrease with increased IMEP [6].

Emissions of uHC in an SI engine are commonly the result of unburned fuel becoming trapped in the crevice volumes of the combustion chamber. As the flame propagates out the increased cylinder pressure forces the fuel-air mixture into crevice

volumes where it is trapped and can only release its energy through post-flame oxidation. In HCCI combustion, crevice volume is still a problem, but uHC in HCCI can also result from delayed combustion and quenching. Low equivalence ratios, resulting in low-load conditions reduce the overall temperature of the combustion reaction. Lower temperatures increase the quenching distance around all surfaces. Results from [6] show a drop in uHC emissions with an increase in IMEP. Figure 2.5 show emissions results for various fuels combusted in an HCCI engine over a range of load conditions.

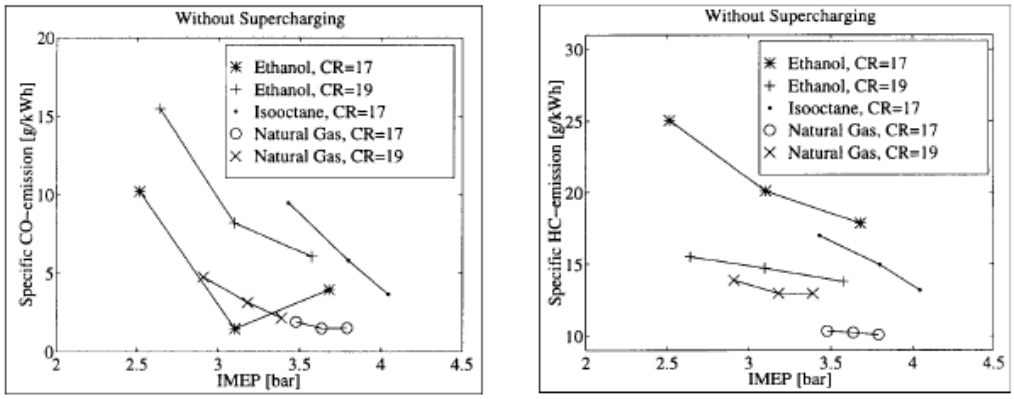

a b

Figure 2.5 CO (a) and HC (b) emissions for various fuels in an HCCI engine over a range of loads [6].

Because of the rapid homogeneous combustion that takes place in HCCI engines, the performance of the engine process is limited. In order to maintain reasonable heat release rates, extremely low equivalence ratios must be used to prevent knocking. Knocking in SI engines is defined as auto-ignition occurring from compression of the mixture that creates oscillations in the cylinder pressure. Since compression ignition is what is desired in HCCI engines, a knocking limit has to be defined to distinguish it from normal operation. A rate of cylinder pressure increase of 10 bar/CA is a common reference for knocking in HCCI

engines and is used as a metric to indicate the potential for mechanical failure. Over a range of speeds this limit was shown to be around an equivalence ratio of 0.2 for n-butane [10]. Due to the lean limits place on operation, HCCI engines are severely limited in power output. This limits the engine's practicality for automotive applications that require a full range of engine load operation.

Cold starting is also an issue hindering HCCI application. Since the ignition is very dependent on temperature history, an HCCI engine starting on cold air will have difficulty firing initially without any preheating or ignition assistance. Glow plugs, SI operation, or increasing the compression ratio through variable compression ratio (VCR) or VVT has been suggested as an initial engine operation aid. Attempts have been made to create "dual-mode" engines that incorporate HCCI combustion into the low load cycles and SI or diesel operation for the remainder of engine operation [1]. This would take advantage of the low load efficiencies of HCCI combustion while avoiding the limitations at moderate and full load caused by its extremely high heat release.

2.1.3. Modeling

Modeling of the HCCI combustion process has gone through several iterations of increased detail as computing technology advances to keep up with suggested CFD and chemical kinetic modeling theories. As detail increases, the accuracy with which these models predict experimental results continues to improve. A model's ability to accurately predict certain observed data does not mean that the model is in fact accurate, though.

A single-zone model for combustion treats the entire chamber volume as isothermal. Calculated pressures and burn rates from single-zone models have been found to be higher

than experimentally observed due to the absence of temperature gradients and boundary layer effects [12]. Modeling parameters for CFD and chemical kinetics can be increasingly detailed without lending any more accuracy to the results using this approach.

Multiple-zone models take into account thermal gradients. Thermal gradients slow the burn rate due to heat transfer through the fluid. As a result lower peak pressures are predicted. These models segregate the mass of the reacting fluid by temperature or some other thermodynamic parameter. In the 10 zone model used in [12], fluid mass was segregated by temperature. Figure 2.6 shows the temperature boundaries used for this mass allocation and the resulting mass fraction in each bin. The predicted pressure trace much more closely matches the experimental results.

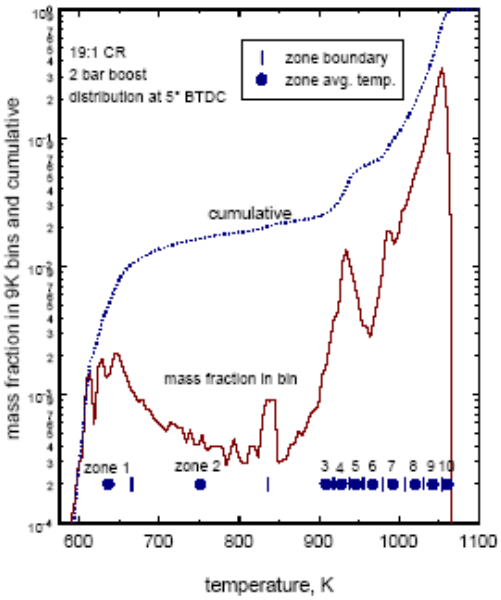

Figure 2.6 Mass fraction and cumulative mass fraction as a function of temperature and mass distribution according to temperature [12].

Three traces are compared in Figure 2.7. The solid line is the experimental data. The two dashed lines represent the two models used to approximate combustion in an HCCI engine. The single-zone model predicts a very high pressure peak because of a lack of thermal gradients. The 10-zone model comes much closer to the experimental data.

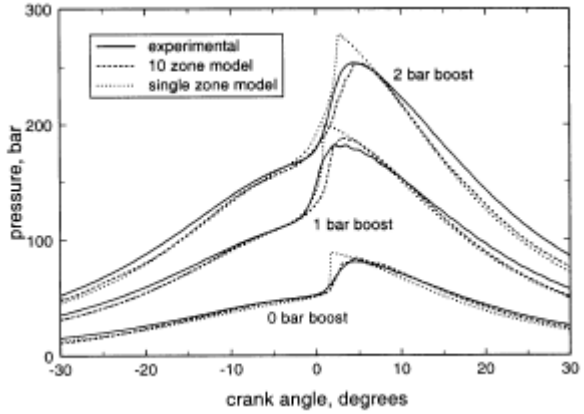

Figure 2.7 Single-zone and 10-zone model and experimental pressure traces for three levels of boost [12].

Near-wall temperatures play a significant role with respect to boundary layer effects during combustion. Quenching occurring in HCCI combustion is strongly determined by the temperature of the fluid near the chamber surfaces. Therefore, it is important for models to accurately predict these temperatures to ensure that near-wall effects are also accurately modeled.

Figure 2.8 from [26] shows the combustion prediction of a 40-zone KIVA3V model. A significant volume of incomplete combustion caused by a large thermal gradient boundary layer effect is predicted.

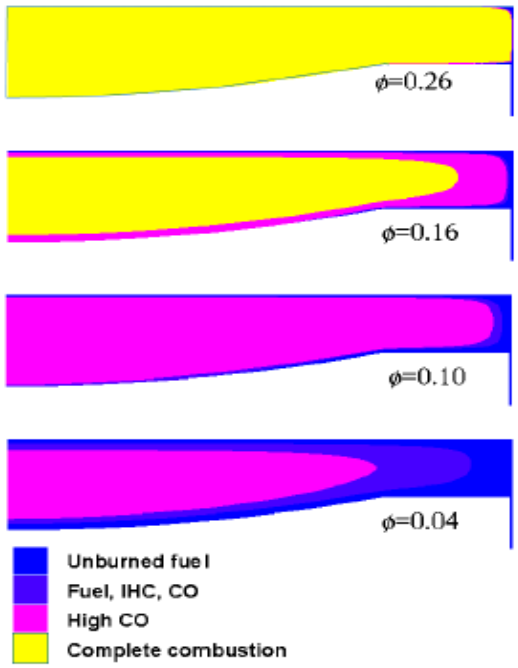

Figure 2.8 Distribution of combustion quality at 6 bTDC for a range of equivalence ratios as predicted by 40-zone KIVA3V model [26].

Figure 2.9 is a plot from [27] of experimentally obtained fluid temperature measurements approaching the cylinder wall at two different crank timings. Both sets of experimental temperature profiles indicate relatively low thermal gradients up to less than 0.25 mm from the wall surface and a cool wall temperature.

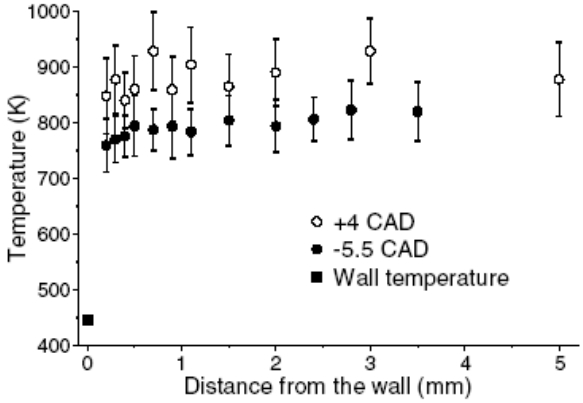

Figure 2.9 Experimental cylinder wall and fluid temperature measurements near the combustion chamber wall. Temperatures taken at two different crank timings [27].

There is an inconsistency between the models used to predict HCCI combustion and the experimental data taken to describe the boundary layer properties. While these multi-zone models have increased the accuracy of pressure trace predictions, the method for doing so may still be flawed. A more precise pressure prediction that fails to accurately describe the actual physical processes taking place in the engine would still need adjustment.

2.2. PLIF

Planar Laser-Induced Fluorescence (PLIF) is an imaging technique used to measure species concentration inside the combustion chamber of an internal combustion engine. It is a non-invasive process that can give quantified temporal and spatial data on various combustion species, temperatures, and densities [15]. A typical setup includes a high power, pulsed laser sheet passing through some flow-field containing a fluorescing species used as a tracer. This results in the absorption and emission of a photon by the tracer species [14]. Images can be taken with a high resolution charge-coupled device (CCD) camera sensitive to the fluorescence wavelength.

2.2.1. Imaging Technique

The concept behind PLIF imaging is to record light emitted by a molecule when it fluoresces. When light of the appropriate wavelength strikes a molecule an electron in its outer shell absorbs the energy from the light and jumps to a higher energy level. The electron then falls back to its original energy level and emits a photon, which is measured for combustion mapping. These images provide a two-dimensional view of reacting species such as OH, CH, or formaldehyde (CH_2O) in the combustion chamber [13].

2.2.2. Laser Selection

Laser selection is critical to achieving quantifiable images from the fluorescing species. Five criteria have been presented for this selection. First, the absorption frequency of the species to be imaged must be obtainable from the laser whether directly or through a frequency-doubling crystal. Second, the spectral distribution of the laser should not represent a significant noise floor compared to the emissions of the excited species. Third, pulse duration should be short enough to temporally resolve flow in the engine. Fourth, pulse power intensity should be large so as to insure a strong enough signal from the fluorescence. Finally, the repetition rate of the laser pulse must be appropriate for the application [16].

2.2.3. Camera

Camera selection is based on several factors discussed in [17] including quantum efficiency, signal-to-noise ratio, and shutter speed. The most common choice for engine flow-field imaging is a CCD camera because of its linearity, low noise, high quantum efficiency, and low cost. However, gate times are not short enough to eliminate combustion luminosity. Image intensifiers are, therefore, coupled to the camera despite the penalty of additional noise and reduced spatial resolution.

CCD cameras consist of an array of pixels or ‘potential wells’ that hold a charge based on the number of photons that impinge upon it. Noise in these cameras is generated from the readout electronics (read noise) and temperature (dark noise). High quality cameras with low noise are cooled significantly to reduce the dark noise.

2.2.4. Processing

There are several factors to consider when using data that has been acquired with the PLIF technique. Some form of data processing must occur to wash out artifacts of the raw image that are not a significant part of the data. For example, extraneous light from other light sources adds to the intensity of the image. One source of extraneous light is background light. It would be very difficult to eliminate all light sources from the room and because the cameras being used for this type of work are very sensitive, small light sources can affect the resulting image intensity. The other unwanted light is from reflections within the combustion chamber. This is partially remedied by painting the cylinder head and valve surfaces flat black. To eliminate any remaining effects, a series of background images are taken and averaged to find a background light level that is then subtracted from the raw images.

Laser non-uniformity is another effect that must be normalized to properly quantify image results. Since the laser sheet is not uniform in intensity across its width, flatfield images are typically taken and averaged to provide a laser sheet intensity profile by which the raw data can be normalized. This process also takes into account attenuation of the light source as it passes through and is absorbed by the fluid in the combustion chamber.

In addition, to ensure that what is being measured as the fluorescing species is not aided in intensity by another interfering chemical, the charge is doped with an additional amount of the imaging species. If the fluorescence intensity increases in proportion to the amount of doping, confidence can be placed in the quantification of the measurements. All images are taken repeatedly and averaged in order to eliminate the presence of shot to shot variation in either the laser or combustion chamber qualities.

2.3. Formaldehyde

Formaldehyde was chosen as the tracer species in this experiment for its significance as an indicator of combustion events in an HCCI engine process and for its appropriate fluorescing properties with respect to the laser and camera used. Formaldehyde is an intermediate species of HCCI combustion using n-heptane fuel. It absorbs light at approximately 355 nm and fluoresces in the visible (~ 425-450 nm).

2.3.1. Combustion Intermediate

The formation and consumption of species in an engine can be used as an indicator of events occurring in the combustion process. For example, during two-stage combustion formaldehyde forms very rapidly during the first low temperature heat release phase. The concentration remains fairly constant until the beginning of the second stage of heat release, during which nearly all of it is consumed [18,25]. This is seen in Figure 2.10.

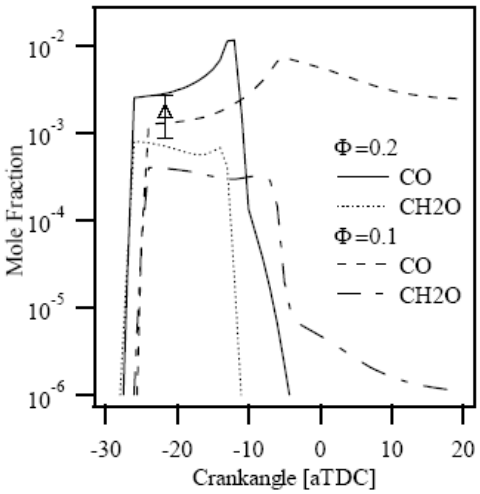

Figure 2.10 Formaldehyde concentrations as a function of crank position for two equivalence ratios [25].

The concentration of formaldehyde therefore indicates the onset of the first and second stages of combustion. These are critical events to know when concerned with controlling the auto-ignition in HCCI combustion. The formaldehyde signal in [18] was confirmed by replacing the ICCD used for imaging with a spectrograph.

2.3.2. Fluorescing Properties

Formaldehyde is a very convenient chemical to use as a combustion indicator for optical purposes. At a wavelength of 355 nm formaldehyde absorbs light and moves to an excited energy state. When energy is released in the form of a photon, it is emitted at wavelengths from 400-550 nm. This light is in the visible range and can be recorded by a sensitive camera. Figure 2.11 is a spectrally resolved formaldehyde fluorescence signal.

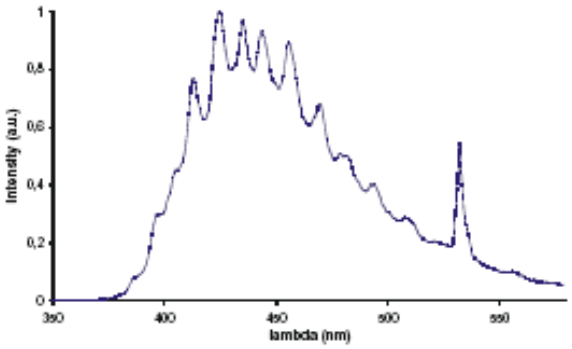

Figure 2.11 Spectrally resolved formaldehyde fluorescence signal [18].

2.4. Near-wall Measurements

When looking at the lean limits of combustion, boundary layer and wall effects can play a significant role in hindering repeatable complete combustion. Cooler wall temperatures can cause delayed oxidation and quenching at larger distances from the wall

than expected. In an HCCI engine, where lean limits are pushed for efficiency and emissions benefits, it is imperative that measurements near the combustion chamber walls be accurate enough to fully explain the effect that these walls have on the periphery of the reacting fluid. Difficulties arise in accessing the boundary layer with conventional diagnostic methods due to their inaccessibility to instrumentation. One method that has been used is rotational coherent anti-Stokes Raman spectroscopy (CARS). This technique measures single point temperatures and was used in [27] to measure fluid temperatures up to about 250 μm from the chamber surface.

2.4.1. Boundary Layer Basics

The boundary layer in a combustion chamber has an impact on both heat transfer and mass allocation for simulation and analysis purposes. Therefore, it must be well defined and understood in order to draw conclusions from measurements taken near the chamber wall. The thermal boundary layer is defined by a set of points where the local temperature is 99% of the fluid temperature [20]. The temperature decreases approaching the chamber wall due to a low wall temperature and heat transfer to the engine block. Some of the literature discusses boundary layers in terms of velocity instead of temperature. The velocity and temperature boundary layers are related through the Prandtl number:

$$\mathrm{Pr} = \frac{\nu}{\alpha}$$

where ν is the kinematic viscosity of the fluid and α is the fluid diffusivity.

For fluids such as gases, the Prandtl number is near unity, meaning that the two boundary layers have approximately equal thickness and can be used interchangeably [20].

A study by Fiveland and Assanis [21] attempted to develop a two-zone HCCI combustion model taking into account boundary layer effects. Their boundary layer model, borrowed from Lyford-Pike and Heywood [22], is based on an SI engine. Measurements taken by Lyford-Pike and Heywood show the boundary layer to increase in thickness through compression and combustion until the exhaust valve opens (EVO) and the layer becomes unstable. A maximum thickness during stable development of approximately 2 mm is reported just before EVO on the side walls. Thicknesses against the cylinder head and piston crown were larger by two to three times. Measurement photographs were taken through the side wall of a square combustion chamber using the schlieren set-up with an accuracy of 0.025 mm.

In a separate study performed in an engine being run under HCCI operation, a similar maximum thickness was measured, however, the development process was found to be different. The boundary layer in this study was shown to decrease through compression and combustion from 1 mm at 90 crank angle degrees (CAD) before top dead center (bTDC) to about 0.5 mm at 30 CAD bTDC [19].

2.4.2. Optics Geometry

The standard methods for PLIF measurements in an engine are not sufficient for near-wall measurements. Normally a sheet of light is passed through an access window in the clearance volume of the engine. A circular window in the center of a Bowditch piston allows camera access from below via a mirror below the piston placed at a 45 degree angle. A more detailed description of a modified method can be found in section 3.3.2.

3. Experimental Setup

3.1. Research Engine

The research described in this thesis was performed on a single-cylinder, optical research engine with an overhead-valve, pushrod cylinder head. The engine was coupled to a regenerative AC dynamometer controlled via a feedback loop. Air was regulated and delivered through a critical orifice and intake surge tank, and fuel was delivered far upstream of the intake port to ensure a homogenous intake charge. A steel spacer ring with integrated quartz windows to allow optical access was located between the block and head. Table 3.1 contains all relevant values of the engine dimensions and timings.

Displacement, [cm^3]	511.0
Bore, [mm]	92.4
Stroke, [mm]	76.2
Clearance Volume, [cm^3]	38.3/60.5
Compression Ratio	14.3/9.4
Connecting Rod Length, [mm]	144.8
Intake Valve Opening, [CAD]	350
Intake Valve Closing, [CAD]	-120
Exhaust Valve Opening, [CAD]	135
Exhaust Valve Closing, [CAD]	370

Table 3.1 Fixed dimensions and timings for GM-Triptane engine. Valve timings are measured from TDC compression.

3.1.1. Base Engine

The engine block used for this study was built and provided by the General Motors Research Laboratory. It was developed in the 1960's for use in conducting alternative fuel studies. The base engine consists of a cast iron crankcase and cylinder bore. The crankcase houses a balancing shaft and a single fixed two-lobe camshaft for actuation of the pushrod valve-train. The cylinder bore was relined to match the diameter of the optical Bowditch piston and contains a liquid coolant jacket.

The piston used was a variable height Bowditch-style piston with an extension below the piston crown and a crown-mounted quartz window to allow for vertical optical access, which was not utilized in this experiment. Since the measurements are to be taken outside the diameter of the window, a different method must be used for fluorescing and imaging the region of interest (ROI). This will be discussed further in Chapter 4.

The piston rings used were manufactured by C. Lee Cook Corporation. The set of four rings included a butt-cut compression ring made of Vespel, two bronze-impregnated rider rings, and an oil ring. Rings were replaced when pressure data and ring thickness measurements indicated. Details of the piston rings can be found in Appendix A.

3.1.2. Cylinder Head, Spacer Ring, Valve Timing

The pushrod-actuated overhead valve cylinder head and extended Bowditch piston used initially gave a compression ratio of 14.3:1. Due to early autoignition the piston assembly was later changed to retard combustion. The resultant compression ratio was 9.4:1. The cylinder head was designed with a flat "pancake" roof with one intake and one exhaust valve. Since the head has been designed for both compression ignition and spark ignition

operation, the centrally located spark plug access hole was plugged. A spark plug was modified so that when installed, it provided a surface flush with the rest of the cylinder head. Another plug was used to seal the fuel injector access. Also installed in the head surface is an AVL model QC42D-E #C109 pressure transducer which was calibrated and used for all pressure data referred to in this thesis. Figure 3.1 gives a bottom view of the layout of the cylinder head.

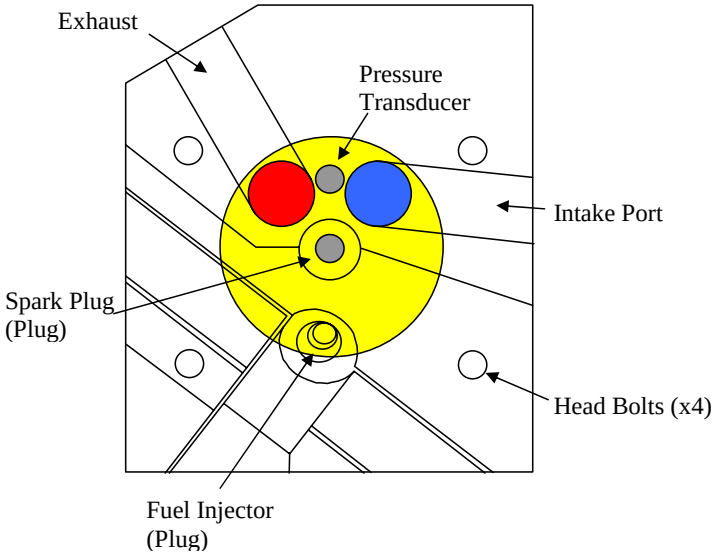

Figure 3.1 Bottom view of the 2-valve pushrod cylinder head [15].

Between the cylinder bore and head is a steel spacer ring used for optical access. The inner diameter matches that of the bore and there are four ports for various engine diagnostic tools located around the ring. In this study only one port was used. A quartz window was installed in the spacer ring for both laser and camera access. The available height for laser propagation and camera access was 14mm. At TDC only 3.05 mm of height is available above the piston. The dimensions and drawing of the window and major engine components

can be found in Appendix B. Seals between the head and spacer ring as well as between the spacer ring and bore were achieved with Viton O-rings.

The valve timing for the engine was set by the single fixed two-lobe camshaft housed in the crankcase. Valves are actuated by two-part pushrods at the engine timings found in Table 3.1. The location of the valve events were confirmed and documented with a graph found in Appendix C.

3.1.3. Peripheral Engine Systems

Associated with the operation of this engine are various systems vital to proper operation and control of the relevant parameters. Discussed in this section will be the dynamometer, oiling system, coolant system, aspiration, fueling, and control systems.

The dynamometer is a three-phase 440 VAC General Electric unit connected to the driveshaft of the engine via a flywheel and coupler. It can be used for both motoring and power generation for operation up to 1500 RPM and loads up to 30 kW. Control is maintained by a Reliance Electric Max Pak Plus VS Drive box and engine speed can be manually adjusted with a rheostat and feedback control loop.

The engine oil is supplied by an external pump at a pressure of at least 45 psi and passes through a commercial filter. The engine oil used is SAE 40 for its higher viscosity, thus helping to prevent oil from bypassing the piston rings and entering the combustion chamber. Penetration into the combustion chamber is especially detrimental for optical reasons. Therefore, a vacuum pump was employed to the crankcase to further control the oil.

The Triptane engine is liquid cooled with a 50/50 antifreeze-water mixture that was maintained at 150°F for all operation. A constant engine temperature removes variance in

heat transfer to the bore and case. Coolant was supplied by an external pump fed from a raised reservoir, and passed through the engine from the head to the block.

Air was supplied to the engine and metered through a critical orifice by adjusting the upstream shop air pressure. Volumetric flow was measured with a bellows meter and a density correction was applied to calculate mass. Calibration of the orifice can be found in Appendix D. Intake pressure was measured with a Wallace & Tiernan model FA 233 pressure gauge at a surge tank between the critical orifice and the engine. One parameter adjusted for this test was intake air temperature. Intake gases were heated with an inline electric heater pipe and controlled with a Love Controls Corporation 1600 Series temperature controller. Intake temperatures were measured immediately before the combustion chamber and were set to range from 50 to 90°C. Exhaust pressure was subjected to a slight vacuum to ensure fumes remained in the exhaust line in case of any leaks developing.

Fuel delivery was accomplished with a custom made, air-assisted fuel injection system. A schematic of the system is detailed in Figure 3.2. An Orbital two-stage injector with an air assisted injection pressure of 80 psi was located 1.3 meters upstream of the intake port for improved fuel vaporization. Nitrogen gas was used to pressurize the liquid fuel in an accumulator, to a pressure of 90 psi. A GO (Model 00-HO2073) pressure regulator maintains the critical pressure differential of 10 psid between the fuel and air to guarantee consistent fueling.

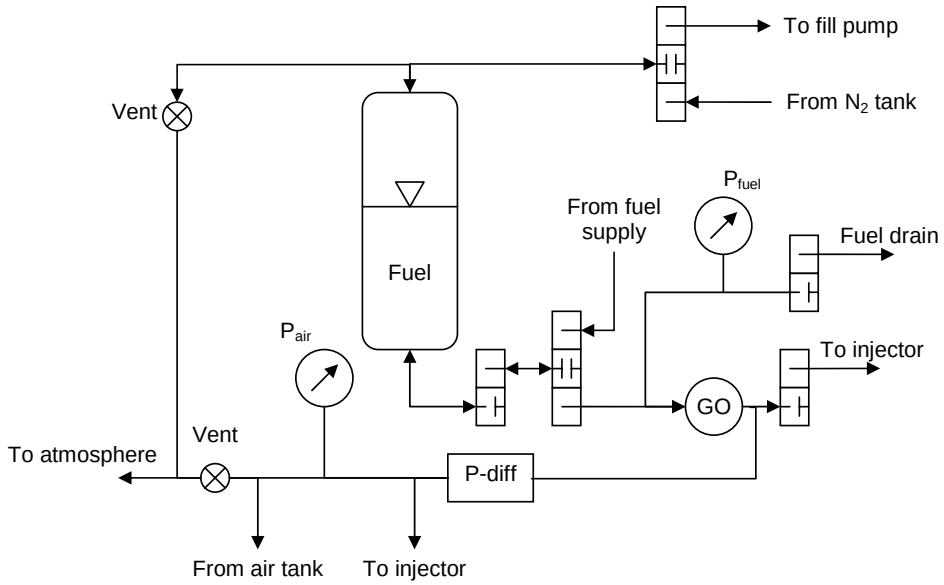

Figure 3.2 Fuel delivery system schematic.

Injection timing and duration are determined by the control program. Since the mixture entering the chamber is homogeneous, fuel injection duration is based on a mass per cycle setting calculated from a desired equivalence ratio. Calibration of the injector flow rate can be found in Appendix E. The injector operates by first injecting the desired amount of fuel into a pre-chamber. Four milliseconds after the fuel is injected, the air-assisted injector delivers the fuel and air mixture into the intake runner with a three millisecond pulse. The injected mixture enters the intake stream counter to the direction of intake air flow to further encourage fuel vaporization. Fuel is stored in a Tobul piston-type accumulator (Model 4.5A20-8-5763) with Teflon seals. Error in equivalence ratio calculation comes from the injector calibration, which was performed in a still air environment, uncertainties in the critical orifice calibration, and leaks both in the intake system and past the piston ring pack.

Control for several of the systems peripheral to the engine was accomplished with MotoTune, a commercially available engine control and calibration program developed by MotoTron. Fuel injection timing and duration, laser firing, camera timing, and a pseudo-encoder used to supply an artificial engine speed for testing without actually running the engine were all handled through this program. MotoTune requires two signals from the engine to determine timing for engine and peripheral system events relative to piston position and stroke. A 60-6 crankshaft encoder and a Hall-effect half-shaft encoder are the two signals generated for the ECU software. The 60-6 wheel is a gear sized for sixty teeth with six of the teeth missing for locating purposes. It mounts to the crankshaft between the dynamometer and the engine with a Hall-effect pickup located radially. The locations of the six missing teeth are recognized by the software for locating the piston position within one revolution [28]. A half-speed wheel is mounted to a half-speed shaft which is connected by belt to the crankshaft. The function of the wheel is to tell the software which stroke of the engine cycle the piston is on. Half of the wheel is cut down to a much smaller radius. The falling edge of the radius, as the wheel rotates, is the second signal used to synchronize the engine control software with the actual engine operation.

An intake seeding system was added to add formaldehyde to the intake air. Increasing the amount of formaldehyde in the combustion chamber would verify that the fluorescence signal was indeed formaldehyde and give a baseline measurement for an approximate known additional amount. Seeding occurred just downstream of the fuel injectors approximately 1.2 meters upstream of the intake port. Formaldehyde was introduced into the intake stream through a porous plug made of sintered metal. A tank of formaldehyde was pressurized with nitrogen for delivery through a micrometer flow valve.

Pressure was monitored immediately upstream of the micrometer valve to ensure repeatable flow rates. Calibration was done outside of the intake runner and a flow rate of approximately 8×10^{-3} cm^3/s was established and repeated. Errors in flow rate may exist due to calibration in a still air environment while seeding for data runs took place within the velocity profile of the intake runner.

3.2. Combustion Data Acquisition

In order to support the optical data taken for this experiment additional engine data diagnostics were measured. Engine pressure data and emissions measurements were recorded for the range of engine operating conditions used for the optical testing. Pressure data were used to analyze and optimize heat release timing as well as measure engine performance for consistency and combustion quality. Emissions measurements were made to correlate emission quality to engine performance and optical measurements.

3.2.1. Cylinder Pressure Data

Cylinder pressure traces were recorded with an AVL model QC42D-E #C109 water-cooled piezoelectric pressure transducer mounted slightly off center of the bore in the cylinder head. A sample pressure trace for motored and fired conditions is shown in Figure 3.3. The surface of the pressure transducer was flush with the bottom surface of the head. Pressure transducer calibration was done with a hydraulic dead-weight tester using a range of weights.

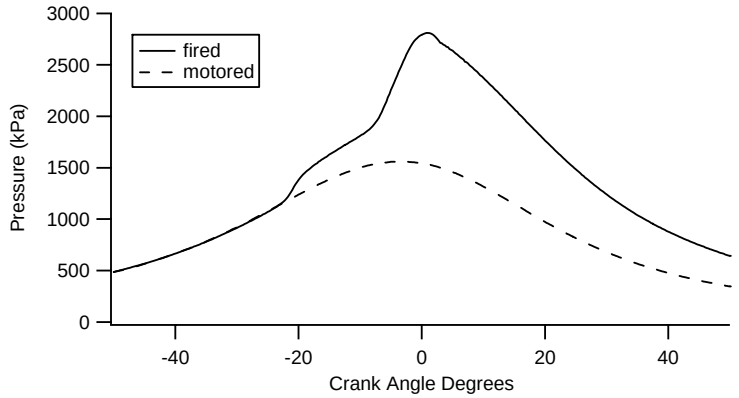

Figure 3.3 Sample motored and fired pressure traces for the Triptane engine using n-heptane.

A least-root-squares fit was made to the calibration with an excellent R^2 value greater than 0.99. The calibration equation and graph can be found in Appendix F. Voltage output from the transducer was run through a Kistler model 5010A12 #C70422 charge amplifier. The amplified signal was input to a Hi-Techniques PC used for A/D conversion that is triggered by a shaft encoder signal with a resolution of 0.25 CAD. The Hi-Techniques computer is also used for interface with the data acquisition software.

The software used was the REVelation program in part of the Win600 package. Basic physical engine measurements were needed for calibrating the software to the specific engine as well as the pressure transducer calibration equation. Each set of pressure data taken consisted of 100 averaged cycles with a trace pegging point of 101.3 kPa at 180° bTDC. Before pressure data were taken for any set of operating conditions, the trace was monitored in real time on a digital oscilloscope to ensure steady state had been reached. Once at steady state, the REVelation data acquisition program was manually triggered for the 100 cycles of recorded data. Each data set is saved as a series of files that are later processed by a C code program to extract the data in a format suitable for spreadsheet display. The data

accessible for analysis includes crank angle, cylinder volume, pressure, and standard deviation of the pressure.

A program written in the Engineering Equation Solver (EES) program was used to model the heat release that occurs in the engine cycle based on a simplified single-zone model. One set of motored pressure data and one set of fired pressure data were taken back-to-back for each running condition. Instantaneous and cumulative heat release curves were calculated based on the difference between these pressure curves. With the current engine configuration, autoignition was occurring too early in the engine cycle. In order to shift the center of the cumulative heat release curve to TDC the piston assembly was changed to give a new compression ratio of 9.4:1. A lower compression ratio retards combustion timing.

3.2.2. Emissions Analyzer

In addition to pressure data, emission gas composition data was also taken to provide a more complete description of the combustion. A Horiba gas analyzer was used to look at species concentrations of CO, CO_2, O_2, uHC, and NOx. Exhaust gas was taken from the intake surge tank through a temperature-controlled line to the emissions bench. The transmission line temperature was set at 190°C to prevent water and uHC from condensing. Prior to entering the analyzers, water is condensed out of the mixture in a 0°C refrigerant bath to give a “dry” composition. Since the Non-dispersive Infrared analyzers (NDIR) used in the Horiba gas analyzer are hygroscopic, meaning they absorb moisture, accuracy depends on dry gases.

Gas concentration is calculated using calibration equations for each of the five measured emissions. An amplifier transforms a voltage signal obtained from the infrared

analyzers with the specific calibration equation. The analyzers for O2, uHC, and NOx have linear transformation equations and therefore only require two points to calibrate. CO and CO2 are both non-linear and were calibrated on a Stec gas divider with a second-order polynomial equation. A program written in LabView 6.0 was used to perform all of the calibration and data acquisition functions for the emissions bench. Table 3.2 provides details for the Horiba gas analyzer.

Emissions Species	Horiba Analyzer Serial Number
O_2	OPE-335
uHC	OPE-435
NO_x	OPE-235
CO	OPE-115
CO_2	OPE-135

Table 3.2 Serial numbers for species analyzers on Horiba emissions bench.

3.3. Optical Setup

The major diagnostic technique of this project was the method of optically measuring flow-field characteristics inside of the combustion chamber known as planar laser-induced fluorescence (PLIF). This technique uses a sheet of light passed through the combustion chamber to fluoresce intermediate combustion species which are then imaged with a highly sensitive camera. In this experiment a wavelength of 355 nm was used to fluoresce formaldehyde.

3.3.1. Laser

The source of laser light for this experiment was a Spectra-Physics GCR-170-10 Nd:YAG laser. This laser outputs a fundamental wavelength beam of pulsed light at 1064

nm and 10 Hz. Integrated with the laser is a Harmonic Generator box near the beam exit port. Frequency multiplying crystals in the Harmonic Generator produce simultaneous and coaxial beams of light at various harmonic frequencies and reduced powers depending on orientation of the crystals. One combination of crystal orientations results in the tripled frequency of 355 nm. Light at this wavelength has a pulse duration of approximately 6 ns and a theoretical maximum power of 220 mJ/pulse. Pulse to pulse stability is optimally <10%. The laser requires two signals for externally triggered operation. The first is a lamp trigger that charges the flash lamp tubes generating a population inversion. At an optimum delay time of 186 ns, a second signal triggers the Q-switch. The Q-switch acts as an electronic shutter or enabler that releases the laser pulse. Laser power for each wavelength was measured after wavelength separation and as near to the input to the engine as possible.

3.3.2. Beam Optics

Light traveling from the laser to the engine passed through a very specific series of optics to isolate the appropriate wavelength, modify the beam shape, and direct the light into the combustion chamber through the small optical access window. Optics were made of fused silica glass due to their strength and transmittance properties of UV light. A diagram of the laser path is given in Figure 3.4.

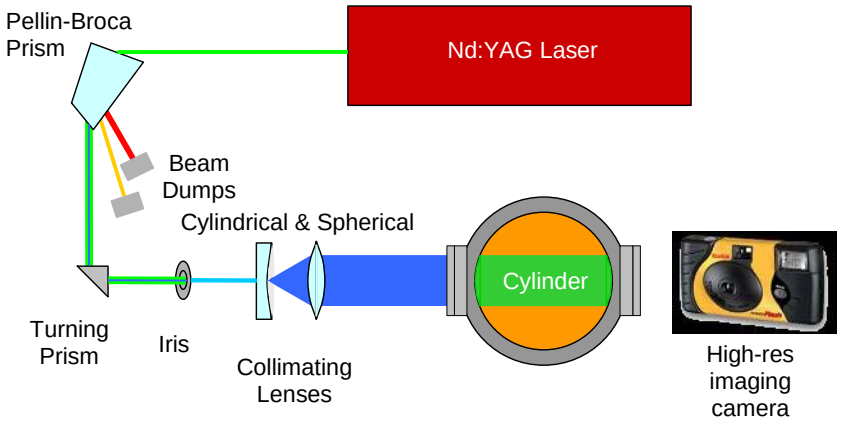

Figure 3.4 Optical setup and path of laser beam.

Light from the laser was turned twice with right angle prisms into a Pellin-Broca prism used for wavelength separation. With the Harmonic Generator crystals arranged to provide 355 nm light, additional light is also emitted at 1064 and 532 nm at powers reduced from their maxima. The Pellin-Broca prism separates light into the individual wavelengths based on different indices of refraction as a function of wavelength. The extraneous visible and infrared beams were dumped but, due to flare of the 532 nm light not all of the visible light is removed. The beam was, therefore, passed through a UG-11 filter that blocks any remaining 532 nm light in the beam. Figure 3.5 show a plot of the transmission of the UG-11 filter as a function of wavelength. The beam was then formed into a vertical sheet with a pair of collimating lenses. First the beam passes through a 500 mm focal length spherical lens, located 500 mm upstream of the desired focal plane. The beam then passes through a +100 mm focal length cylindrical lens with a horizontal axis for the radius of curvature. The light is formed into a sheet with a gradually increasing height and a horizontal waist at the focal plane.

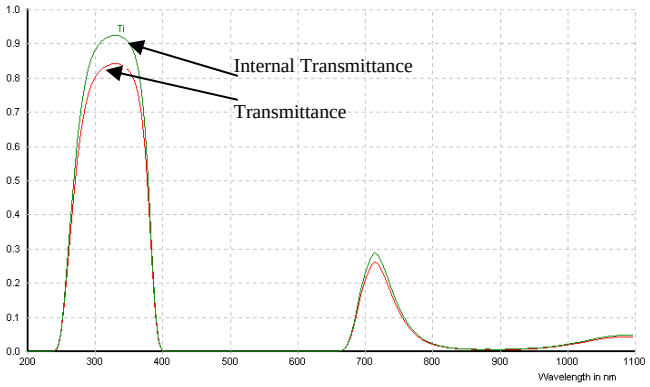

Figure 3.5 Transmittance plot for UG-11 filter [30].

The laser sheet passes into the engine through the engine spacer ring window. This window accesses the clearance volume of the engine with field of view being clipped by the piston near TDC. The laser enters the window at an angle of 31.2° and therefore propagates through the combustion chamber at the same angle. This angle gives lateral and depth resolution in the image. Viewed by the camera, the light passes through the engine from left to right. Therefore, at the left edge of the field of view where the light has exited the window, the laser sheet is very close to the internal window surface. As the laser moves to the right, it also moves deeper into the cylinder. By measuring the angle of the laser incident on the window, we can determine a relationship between horizontal pixel distance and depth away from the cylinder wall. Figure 3.6 shows the laser path into the engine. As a result of the angled laser sheet, problems with flare off of the window surfaces, depth of field, and field of view become significant. These will be addressed in Chapter 4.

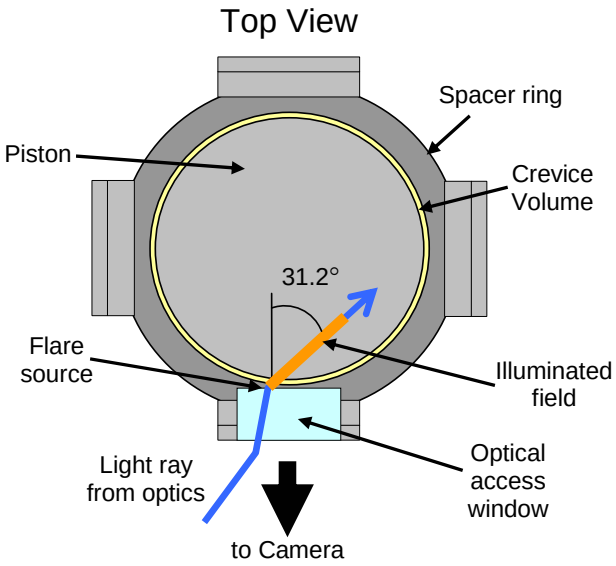

Figure 3.6 Top view of the spacer ring and piston. Path of laser into the combustion chamber through the optical access window.

3.3.3. Camera

The camera used for the bulk of this project was the Roper Scientific PI Max intensified charge-coupled device (ICCD) with a 512 × 512 array of 24 μm pixels. This is a full frame, front illuminated camera cooled to -20C for reduced dark noise. The camera was operated by the WinView/32 v. 2.4.8 program developed by Princeton Instruments. Each pixel, or 'potential well', collects photons and stores them as an intensity. In order to read out the data the entire image is first shifted up one row, delivering the top row to the serial register which outputs to an amplifier. This is done with an extremely high efficiency (~0.999998). Figure 3.7 shows a CCD schematic. The CCD in this camera is also intensified.

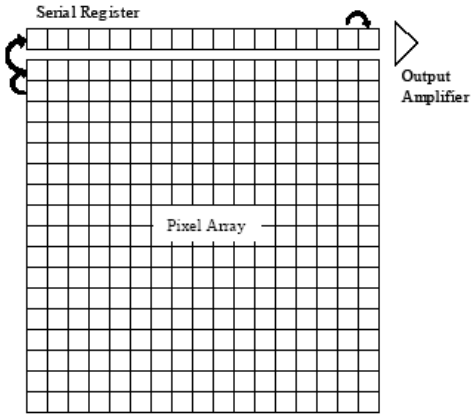

Figure 3.7 CCD pixel array diagram [17].

An image intensifier consists of a photocathode and a phosphor screen separated by two gaps and a microchannel plate (MCP). When a photon hits the photocathode an electron is accelerated across the first gap to the MCP where it is amplified and then transferred across the second gap to the phosphor plate for imaging. Although this amplifies the image intensity, it also increases the noise level associated with the data and includes a related quantum efficiency. The readout rate for this camera was 0.1 or 1.0 MHz with a digitization of 14 bits and an overall quantum efficiency of 31% [17].

This camera was chosen for its ability to achieve a high signal-to-noise ratio for the weak formaldehyde images that were expected. For this project the exposure time was set to 200 ns. The lens used with this camera was an 85mm Nikkor $f/1.4$. This lens was chosen because it gave a relatively large image size, which equates to higher resolution, while maintaining an acceptable depth of field with the help of one 12 mm extension tube. At a distance of 225 mm between the back surface of the optical access window and the front of the camera lens, magnification was approximately 0.42. A pair of filters was placed

immediately in front of the camera lens to block flare from the 355 nm light, ambient room light, and flash from the 532 nm laser light that was not completely dumped. Both filter had a transmission of about 90% at 425-450 nm where formaldehyde emits.

3.3.4. Timing System

Timing of the laser and camera are achieved by using the available spark signals generated by the ECU to delay and trigger the various events. Two spark signals were needed to time the laser with the engine. The laser operates at a frequency of 10 Hz and will fire off of an external signal when that signal is received at a frequency of approximately 10 Hz. For this reason the engine was run at 600 or 1200 RPM. However, at 600 RPM, where all significant data for this project was taken, a spark signal would only occur once every other revolution or at 300 RPM. Therefore two spark signals are used and offset by 360 degrees. The two spark signals, each at 5 Hz, are combined by an OR gate that outputs a single 10 Hz signal. This signal is then used as an external trigger for a BNC Berkeley Nucleonics model 555 pulse/delay generator that outputs signals to the laser and camera. The laser requires two signals. The first signal is for the flash lamps and causes excitation of the flash lamps. After a delay of approximately 200 μs, the second laser signal triggers the Q-switch. The third signal from the BNC pulse/delay generator is used to indirectly trigger the camera. Since the camera cannot operate fast enough to match the speed of the engine and laser, it was uncertain which spark signal the camera would use to image for each exposure. This means that some images could be taken 360 degrees off of the desired crank angle timing. To remedy this, a One and Only One logic box was used. The One and Only One processor requires two inputs. The first is called a clock signal and comes from the

spark signal associated with the crank angle of interest. The second signal is the normal camera trigger acting as an enabler signal. The One and Only One box outputs a signal that triggers a Programmable Timing Generator (PTG) which has several parameters manipulated by the camera control software WinView32. Within WinView32 an additional delay can be set as well as exposure time. The PTG along with a controller, trigger the camera operations. Additional experiments were performed to determine all the delays inherent to the system such as signal delay, processing time and light travel delay. These times had to be measured very accurately as laser pulse duration was on the order of a few nanoseconds. Figure 3.8 shows a schematic for the timing system signal processing.

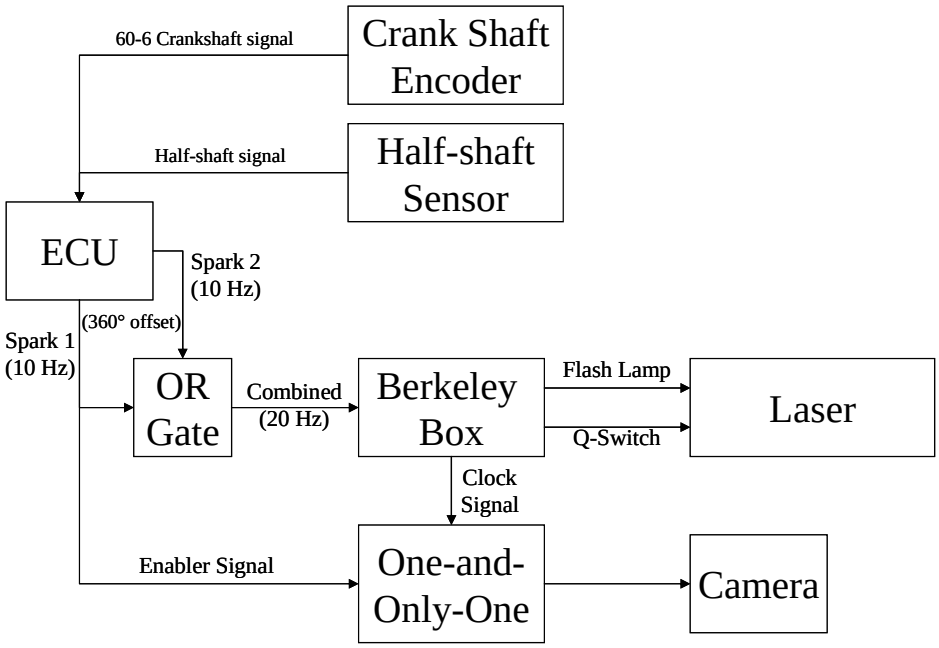

Figure 3.8 Diagram for timing signal processing.

4. Optical Obstacles

Several optical issues were anticipated and arose during this project that affected the quality of the image data. These additional challenges were, in large part, the result of the method for near-wall optical access that was being attempted. Normally, optical access for in-cylinder measurements is accomplished with a Bowditch-style piston. This piston has a window mounted in the crown of the piston and an extension below with a 45° turning mirror near the bottom of the piston that provides access to the combustion above. It is visible to a camera through a hole in the side of the bore. A sheet of light is passed across the clearance volume of the combustion chamber through another access window in the spacer ring. Light from fluorescing species follows a path through the center of the piston, turning at the mirror, and exiting to the camera. A diagram of this arrangement is found in Figure 4.1.

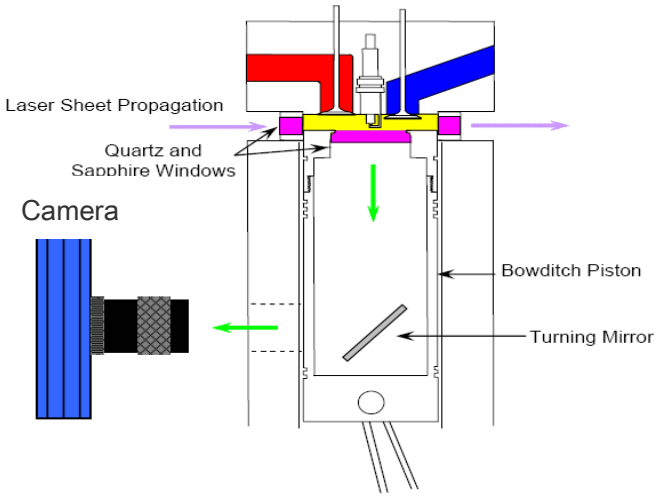

Figure 4.1 Diagram of conventional access of the combustion chamber in an optical engine using an extended Bowditch piston [15].

Since the desired measurements are to be taken outside the diameter of the piston-mounted window, a different method was necessary for exciting and imaging fluorescence from the region near the wall. Figure 4.2 illustrates the piston as an obstruction with conventional chamber access methods.

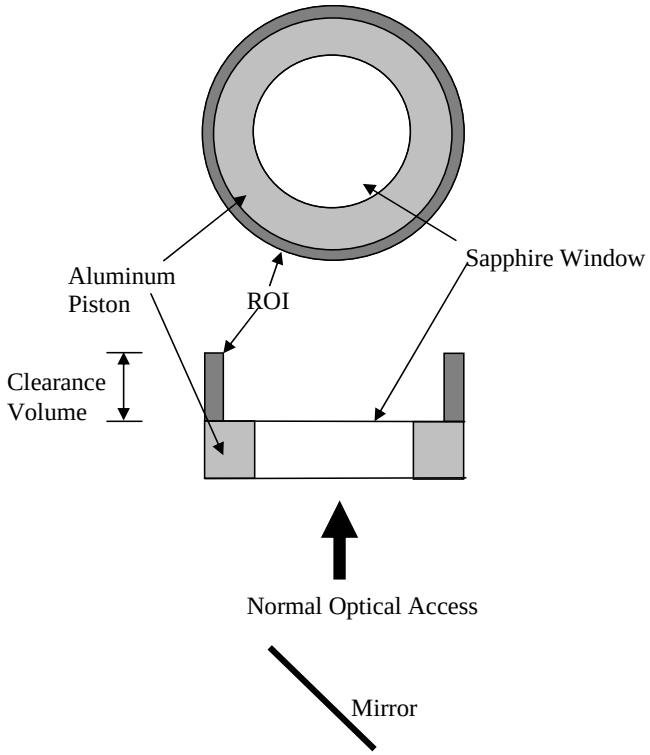

Figure 4.2 Piston as an obstruction to standard optical access for the region of interest.

Another configuration that has been attempted is to attach a square piston and cylinder head to the top of the standard engine. One of the sides is then made into an optical window for easy access to the combustion chamber [22]. However, this has the potential of affecting combustion characteristics including fluid flow and peripheral heat transfer. In this project the imaging camera will access the combustion chamber through the same window that the laser sheet passes through.

The most significant difficulty resulting from the crowded optical probing and access was an optical phenomenon called vignetting. Vignetting is the loss of image intensity near an obstruction of the light source in an image field. In this project, vignetting was a concern near the piston crown surface and near the edge of the spacer ring window housing. The initial method of chamber access involved passing a vertical sheet of light through the middle of the combustion chamber as seen in Figure 4.3.

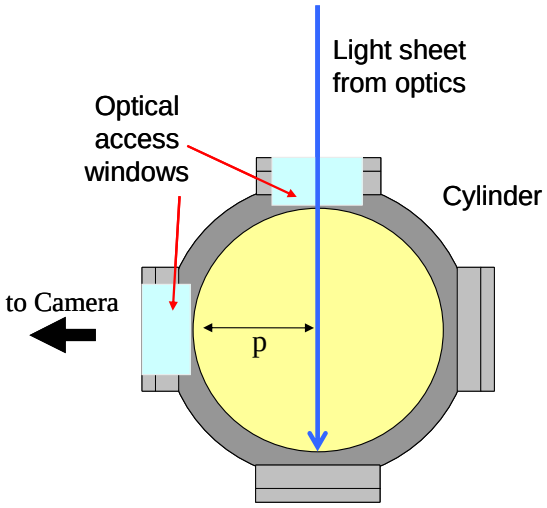

Figure 4.3 Initial method of optical access for near-wall measurements.

Near-wall measurements would be made close to the piston head surface. The problem with this method was, in order to image this field, the camera must 'look' across the entire piston radius in addition to the spacer ring and window mounting bracket. It will be shown subsequently in this chapter that this distance, *p*, would have the effect of corrupting the data near the piston surface, where this study is most concerned. The second issue that was dealt with regarding optical measurements was flare. Flare results when light scatters off an imperfect surface such as the fused silica windows used in the optical access piston ring

window. When the laser sheet passed through the window, flare occurred at both the inner and outer faces of the window as the light sheet passed from one optical medium to the next. At the locations of reflection the imaged intensity due to flare could be far brighter than that of the fluorescing formaldehyde in the engine, overshadowing the desired data. The third issue dealt with was depth of field. Depth of field is a measure of the distance removed from the focal plane an object can be while remaining in focus. Focal length of the camera lens, aperture size, and object distance all affect the depth of field of an image. For our purposes image size and thus resolution was also an important result.

4.1. Vignetting

Vignetting is an optical phenomenon that causes the edges and corners of an image to darken. This effect is more prominent at larger apertures [23]. Since the largest aperture possible will be used to obtain the maximum amount of light from the in-cylinder images, and the data quality relies on the accuracy of image intensity as an indicator of the concentration of the species being illuminated for observance, the vignetting effects must be examined and quantified to determine the extent of their effect. Figure 4.4 shows the effect of vignetting when a brick wall is photographed with two different size apertures.

Figure 4.4 Vignetting seen in a photograph for two aperture sizes. Left: *f*/1.4. Right: *f*/5.6 [29].

The left side was photographed with an aperture of f/1.4. You can clearly see the corners of the image are darker than the center. The right half was imaged with an aperture size of f/5.6. In this image the vignetting has been practically eliminated with the use of a smaller aperture.

When data images are taken in an optical engine cylinder, it is very important that the intensity of the image be accurate throughout the field of view. Image intensity was an indicator of the concentration of formaldehyde in this project. Therefore, vignetting must be studied and taken into account when examining any images quantitatively.

4.1.1. Vignetting Forms

There are three forms of vignetting that contribute to the gradual transition in intensity of an image. Optical and natural vignetting are both inherent to lens and object geometry and are thought to have an insignificant effect on in-cylinder images. The third form of vignetting is caused by an obstruction between the light source and the camera. Obstruction vignetting is significant in this experiment and was quantified.

Optical vignetting is the result of a lens having a length. Light entering from an angle sees less of the full cross-sectional area of the lens due its incident angle. In addition, at distances further off of the optical axis, the exterior of the lens housing blocks a portion of the rear of the lens assembly. Figure 4.5 illustrates this effect and shows that it is much more prominent with larger apertures causing the effect to be more pronounced in the image. The white openings are the areas light is able to pass through.

Figure 4.5 Optical vignetting as a function of aperture size. Left: *f*/1.4. Right: *f*/5.6 [29].

It is apparent that less light is collected by the camera as an object is placed further to the outside of its field of view causing the edges of the image to dim. Optical vignetting, in effect, decreases the size of the aperture being used for the affected areas.

Natural vignetting occurs internal to the lens and is a function of the angle at which the light impinges upon the light sensing surface from the exit pupil. The drop-off in intensity is a function of a $\cos^4$ term [29]. There are three contributions to this term. First there is a $\cos^2$ factor due to the inverse square law associated with the longer distance traveled by the light to get to the corner of the image from the lens pupil. Second, the pupil created by the aperture stop is elliptical in shape to the corner of the image unlike the circle seen by the center. This is similar to the optical vignetting that occurs externally and results in another cos term. Third, light hitting the edges of the developing surface strikes it at an acute angle instead of normally. Therefore, a similar amount of light to that striking the center of the image, is spread over a larger area when is hits the edge of the image. This last effect is known as Lambert's law and contributes the last cos term. These three effects combine to produce a $\cos^4$ illumination falloff. Figure 4.6 illustrates the difference between two cones of light impinging upon the center and the corner of the image.

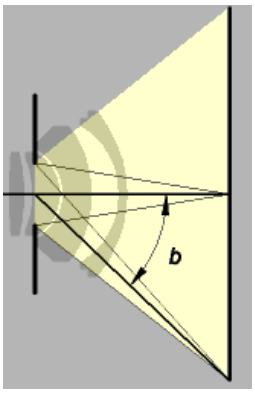

Figure 4.6 Natural vignetting as a function of a light source's distance removed from the optical axis [29].

The third form of vignetting is a result of the obstruction placed in front of the light source. Immediately next to the obstruction boundary, the light source will appear to dim and increase gradually to its maximum value moving away from the obstruction. The light source appears dimmer due to a portion of the light being blocked by the obstruction. Figure 4.7 illustrates this form of vignetting. The upper cone of light, from a point on the light source not affected by vignetting, represents light that is visible to the entire cross-section of the camera lens. The light from directly above the obstruction, however, is limited to a portion of the camera lens area. This does not allow for the same amount of light to be absorbed and therefore the image dims as it approaches the obstruction boundary.

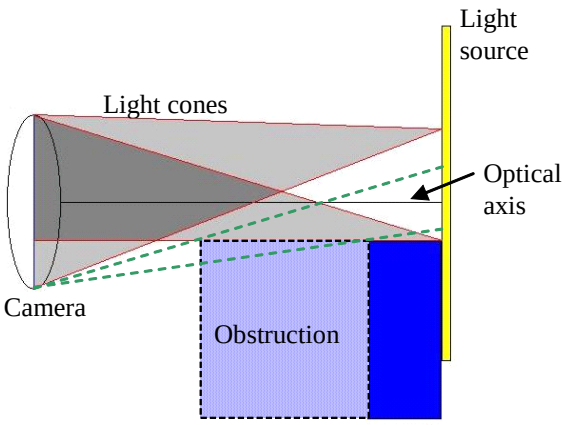

Figure 4.7 Diagram of proposed obstruction vignetting.

As the point source of light moves up away from the obstruction, more of the camera lens is utilized causing the vignetting to decrease in severity. With deeper obstructions, the theoretical height of the light source area that will be affected by vignetting increases. Another observation that can be made is that an increase in obstruction depth will increase the severity of vignetting effect on the light intensity immediately next to the obstruction boundary. A prediction of the height of the affected area can be arrived at through simple geometric calculations.

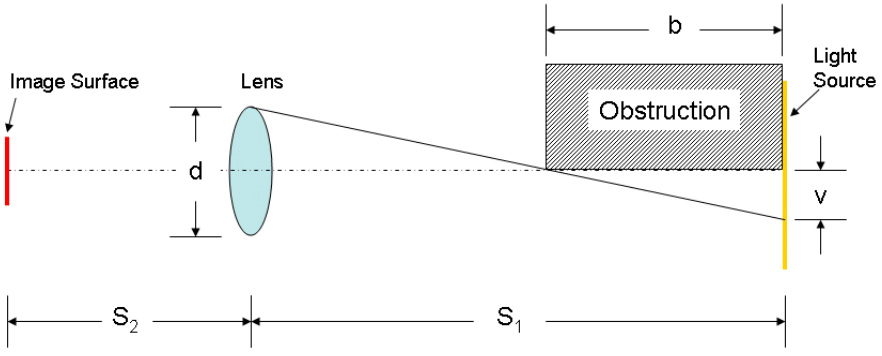

Figure 4.8 Diagram of dimensions for vignetting distance prediction equation.

For purposes of simplification, we will assume that the camera lens assembly consists of one lens of the given focal length and a diameter, *d*, based on the aperture calculation *f/x*, where *x* is the aperture setting. With known light source dimensions and camera CCD pixel size, a magnification, *M*, for any image can be calculated. Using basic lens equations, we can get an effective location of the approximated single lens within the lens housing. Figure 4.8 illustrates all the important dimensions for arriving at a prediction for the height of vignetting effect, *v*. The following equations describe the geometric prediction of the depth of the vignetting effect.

$$v = \frac{b * d}{2 * \left(\frac{l}{M + 1} - b \right)} \qquad \text{where: } M = \frac{S_2}{S_1} \text{ and } l = S_1 + S_2$$

4.1.2. Vignetting Measurements

A supplementary experiment was performed to investigate image data near an obstruction is affected depending on the depth of the obstruction. Two setups were used for this test. First, an LED array with a diffusing surface was used to provide a near-uniform light source. Power was supplied by a variable DC voltage source. The second light source was PLIF from a 10 x 10 mm cuvette filled with methanol-diluted rhodamine dye that was illuminated by an Ar^+ laser. Light from the laser was formed into a sheet using a 10 mm cylindrical lens and a 500 mm spherical lens. Mirrors directed the beam to the cuvette. The dye mixture was diluted to allow light to pass completely through the cell, causing fluorescence across the entire width of the cell. This second setup provided a light source more similar to that found in engine PLIF images.

An Apogee AP7 CCD camera was used with a 105mm Nikon lens set at an aperture of f/2.8 to record the images. Pixel size for this camera was 24 μm. For focusing purposes, a razorblade was taped to the front surface of the light source. This provided a sharp line of contrast on which to focus the camera.

The obstruction in the engine that will be responsible for the vignetting effect is the piston crown. It was simulated in this experiment with a series of parallels placed immediately in front of the light source being imaged. The vignetting effect was expected to be dependent on the depth of the obstruction. In the engine, the deepest possible obstruction is the piston radius plus spacer ring thickness totaling 67.3 mm. Each parallel used was 12.7 mm (0.5") deep. In order to determine the effect of the piston, in this experiment the maximum obstruction depth was bracketed. A series of images were taken with zero, one, three, five, and seven parallels to provide a base image, 12.7, 38.1, 63.5, and 88.9 mm (0.5, 1.5, 2.5, and 3.5") obstruction images respectively.

For the uniform light source, a set of forty background images were taken with the light source off. Then five flat-field images were taken with the light source illuminated. The obstructions were placed on a stand horizontally in front of the light source, and vignetting was measured from the plane of the top surface of the obstruction upwards.

For the PLIF-illuminated cuvette, twenty background images were taken followed by ten flat-field images. Obstructions were placed vertically in line with the razor to verify the obstruction boundary location. Vignetting was measured horizontally. Intensity falloff was associated with vignetting near the obstruction as well as attenuation due to absorption by the dye.

Image post-processing was done and further data analysis was performed using various commercially available image processing and graphing software. Each set of background and flat-field images were averaged to remove any aberrations that developed as a result of imperfect imaging. The background images were then subtracted from the flat-fields to produce images representative of only the additional light produced by the two light sources. The formula below represents the initial post-processing procedure for the uniform light source.

$$IMAGE = \left[\left(\frac{1}{n_f} \sum_{i=1}^{n_f} f_i \right) - \left(\frac{1}{n_b} \sum_{i=1}^{n_b} b_i \right) \right]$$

where: n = number of images
b = background
f = flat-field

In Figure 4.9, the 12.7 mm obstruction is placed horizontally near the bottom and a razorblade is placed vertically, immediately against the uniform light source for focusing and comparison purposes.

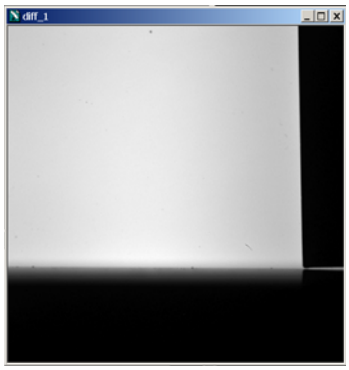

Figure 4.9 Sample image from vignetting experiment. Right: razor blade. Bottom: 12.7 mm obstruction.

Vignetting seems to be present just above the boundary of the obstruction where the light source dims. Next to the razorblade there is a much sharper contrast across the edge of the blade. However, there are other light intensity variables to consider before drawing

conclusions. While the light source is designed to be uniform, there are most likely brighter and dimmer areas. Also, the previously discussed optical and natural vignetting must be taken into account. In order to eliminate the optical and natural vignetting that occur independent of obstructions, and eliminate non-uniformities in the light source, the averaged image with the obstruction is divided by the averaged image with no obstruction. Below is a formula for the corrected image.

$$IMAGE = \frac{\left[\left(\frac{1}{n_{f,0}} * \sum_{i=1}^{n_{f,0}} f_i\right) - \left(\frac{1}{n_{b,0}} * \sum_{i=1}^{n_{b,0}} b_i\right)\right]}{\left[\left(\frac{1}{n_{f,m}} * \sum_{i=1}^{n_{f,m}} f_i\right) - \left(\frac{1}{n_{b,m}} * \sum_{i=1}^{n_{b,m}} b_i\right)\right]}$$

where: n = number of images
b = background
f = flat-field
0 = no obstructions
m = number of parallel obstructions

This formula will provide an image scaled in intensity from zero to approximately one. A value of zero indicates that light from that portion of the image has been completely blocked by the obstruction. A value of one means that light from that area of the image with the obstructions equal in intensity to the light from that area in the image without the obstruction. Equal intensities indicate that vignetting has no effect in this area. Vignetting appears in these images of the uniform light source as a gradual brightening moving away from the line of the obstruction due to the above pixel intensity math. The image and corresponding intensity graph in Figure 4.10 are of the uniform light source with a 12.7 mm obstruction normalized by the image of the light source with no obstruction. This image shows that light from the obstructed source was equal to or greater in intensity to the light from the unobstructed source over a large portion of the image. In the line profile graph, up to approximately 0.75 mm from the boundary surface, the relative intensity is less than one.

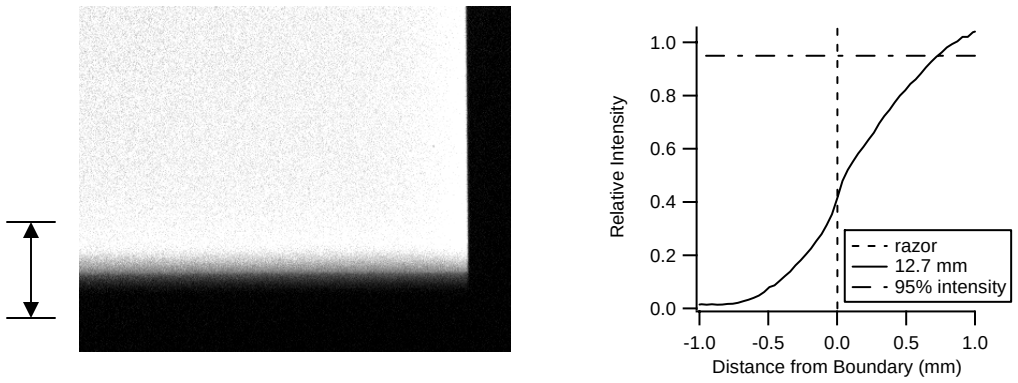

Figure 4.10 Image and intensity profile, for indicated range, of a razor blade and 12.7 mm obstruction placed in front of a uniform light source. In the plot, vignetting exists to the right of the vertical dashed line.

At the obstruction boundary, represented by the vertical dashed line, the intensity does not drop immediately to zero as might be expected. The reason for a significant amount of light present below the obstruction boundary is the possibility of reflection of the light off the top surface of the obstruction. If we define vignetting to be significant when it has at least a five percent effect on the unobstructed intensity, then vignetting is present in these images up to the pixel where the intensity curve intersects the dashed ninety-five percent line in each graph. Vignetting is observable in the image with a 12.7 mm obstruction for about 0.75 mm. A series of images were taken with obstruction of 38.1, 63.5, and 88.9 mm placed in front of the uniform light source. In the following sets of images, vignetting affected an increasingly large distance off the boundary as the obstruction placed in front of the light source became deeper. When compared to values predicted by the geometry relationship described earlier, the experimental results lie below the predicted values by a factor ranging from about 2 for the 12.7 mm obstruction to about 1.1 for the 88.9 mm obstruction.

Plotting each curve for the four obstruction thicknesses illustrates the significant difference in rate of falloff of the light and vignetting distance. Vignetting, in Figure 4.11, lies to the right the obstruction boundary at zero.

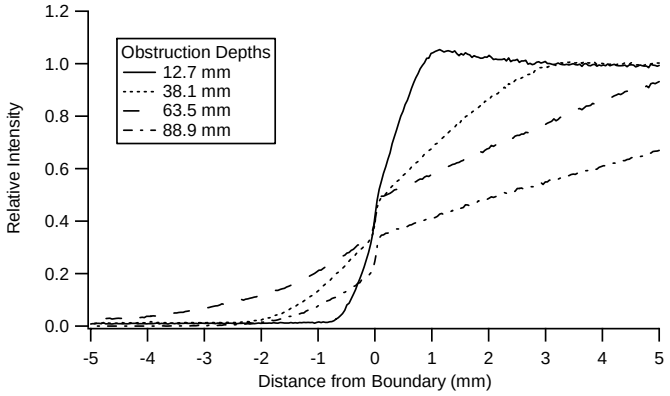

Figure 4.11 Plots of relative intensity vs. distance away from the obstruction boundary for four obstruction depths (12.7, 38.1, 63.5, 88.9 mm).

The slopes of the intensity decay become increasingly gradual as the obstruction depth is increased. For further analysis, the range of each intensity trace was normalized by the predicted vignetting effect value of each respective obstruction depth. The traces were then shifted so that each point with intensity of 0.5 was aligned. This resulted in the plot in Figure 4.12 that shows a fairly common slope for each curve.

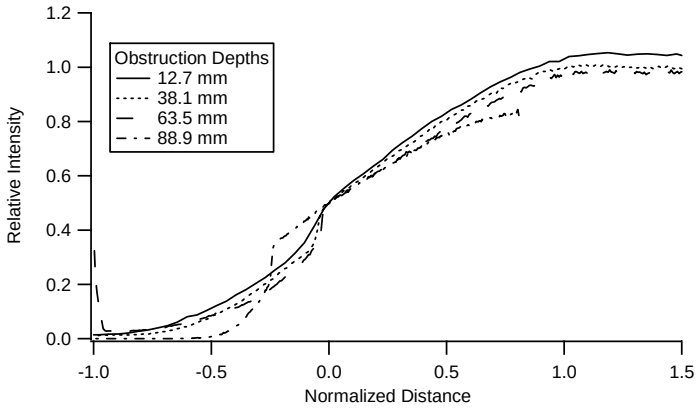

Figure 4.12 Relative intensity as a function of distance from the obstruction boundary normalized by the predicted vignetting distance for the uniform light source and four obstruction depths (12.7, 38.1, 63.5, 88.9 mm).

The fact that these slopes align indicates that a simple factor may be applied to the previously developed equation for predicting the actual amount of vignetting that occurs as a function of obstruction depth.

For the sets of images taken with the PLIF-illuminated dye light source, the same post-processing image math was used to develop the data to be analyzed. Normalizing the obstructed image with the unobstructed will yield a data image that exhibits dimming of the light source departing from the obstruction boundary and scaling from zero to approximately one. In addition, for this set of data, a razor edge was placed in the same plane as the obstruction boundary to give a direct view of the effect of vignetting in each case.

With a 63.5 mm obstruction in front of the light source, vignetting can be observed across the area of the cuvette not blocked by the obstruction to the right of the dashed razorblade profile in Figure 4.13. This figure shows the corrected image and associated line profile window for a 63.5 mm obstruction placed vertically in front of the light source. It is clear in the image where the razorblade ends and the vertical obstruction begins.

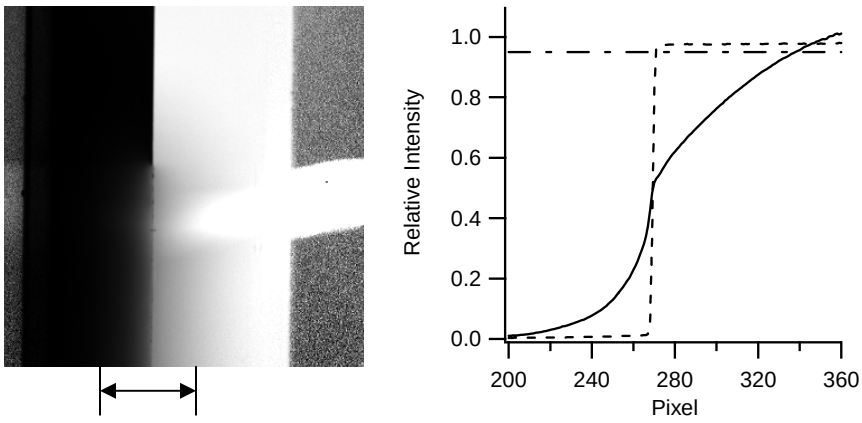

Figure 4.13 Image and intensity profile, for indicated range, of a razor blade and 63.5 mm obstruction placed in front of a PLIF illuminated, dye-filled cuvette light source. In the plot, vignetting exists to the right of the vertical dashed line.

The razorblade exhibits a sharp line between dark and light that ends about two thirds of the way to the top of the field of view. The obstruction begins where vignetting becomes apparent with the blurring of that line. An anomaly occurred in each of the post-processed images in the form of a very bright horizontal band of light extending from the obstruction boundary to the right edge of the field of view at about the middle of the image. This may be the result of an imperfection in the obstruction surface that caused a large amount of reflection of the fluorescing light. It is otherwise unexplained. In addition, all four of the intensity plots rise above a value of one. This could be another indication of stray reflection affecting the intensity of the illuminated side of the image as well. When looking at the line profile graph for the image, the same plot format is used as in the uniform light source images. The solid line represents the intensity profile across the obstruction boundary. The dashed line with a sharp vertical climb indicated the intensity drop-off across the razorblade edge. Finally, the horizontal dashed line indicates the ninety-five percent value at which vignetting is considered to have a significant effect on the image intensity. Also, similar to the uniform light source, the image intensity does not drop off immediately to zero to the left of the obstruction boundary. This is most likely again due to reflection off the obstruction surface. Vignetting exists in Figure 4.13 from the boundary surface, found with the razorblade edge at zero, to the intersection with the ninety-five percent line about 3.75 mm away from the boundary. Again, the other data images with varying obstruction depths exhibited the same increase in vignetting distance with an increase in obstruction depth.

Plots of all four cases were again developed to directly compare the differences in vignetting effects. Figure 4.14 illustrates the different rates at which vignetting effects decay to the right of the sharp intensity increase. It can be seen again that as obstruction depth

increases, vignetting becomes more significant at the boundary and extends further into the unobstructed field of view.

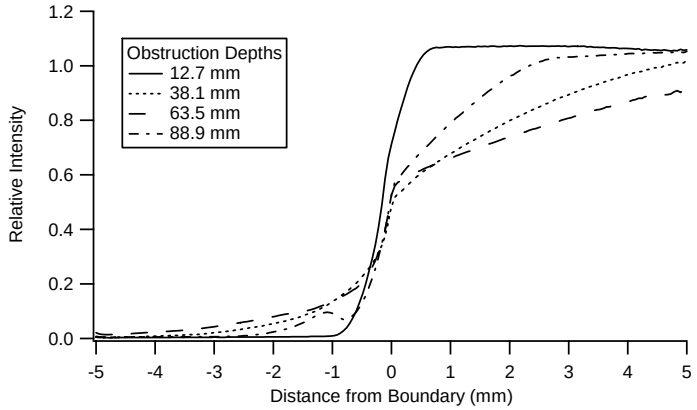

Figure 4.14 Plots of relative intensity vs. distance away from the obstruction boundary for four obstruction depths (12.7, 38.1, 63.5, 88.9 mm).

The curves were again normalized by the predicted pixel distance of the vignetting effect. Curves were then shifted along the pixel axis to align each where it crossed the relative intensity of 0.5. Figure 4.15 shows how the slopes once again fall on top of one another where vignetting takes place.

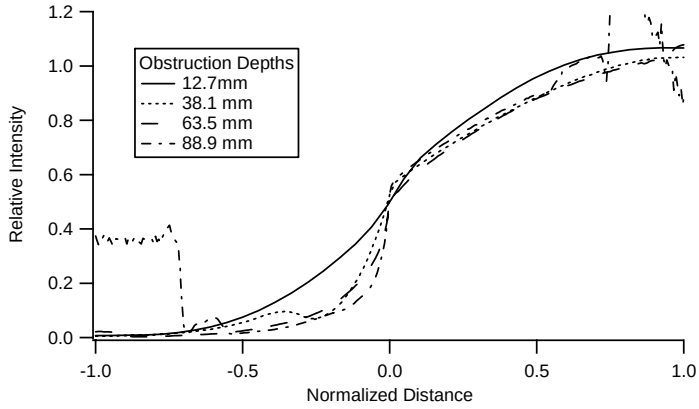

Figure 4.15 Relative intensity as a function of distance from the obstruction boundary normalized by the predicted vignetting distance for the PLIF illuminated light source and four obstruction depths (12.7, 38.1, 63.5, 88.9 mm).

Table 4.1 summarizes the results for the four different obstruction depths. Variables *b* and *v* represent the boundary thickness and resulting vignetting distance respectively according to the vignetting geometry equations described earlier. The variable v_{95} is ninety-five percent of the predicted vignetting distance. Since we took vignetting to exist where light intensity was at ninety-five percent or less, a fraction of the predicted value should be used for comparison purposes. $Pix_{u,a}$ and $pix_{u,b}$ are absolute pixel locations for the beginning and end of vignetting in the uniform pixel images. $Pix_{p,a}$ and $pix_{p,b}$ are the corresponding variables for the PLIF images. V_u and v_p are the experimentally found vignetting distances for the uniform and PLIF images. Finally, rat_u and rat_p represent the factors by which the measured values, v_u and v_p, are different from the predictive geometry values.

Obstruction Depth, b (mm)	Vignetting Distance, v (mm)	v_{95} (mm)	$pix_{u,a}$	$pix_{u,b}$	$pix_{p,a}$	$pix_{p,b}$	v_u (mm)	v_p (mm)	rat_u	rat_p
12.7	0.9110	0.8654	250	231	275	266	0.456	0.216	1.9	4.0
38.1	3.0270	2.876	250	181	304	269	1.656	0.84	1.7	3.4
63.5	5.6535	5.371	250	110	338	269	3.36	1.656	1.6	3.2
88.9	9.0004	8.55	250	-77	365	269	7.848	2.304	1.1	3.7

Table 4.1 Vignetting calculation results summary for obstruction depths generated by 0.5, 1.5, 2.5, and 3.5 inch gauge blocks in front of a PLIF-illuminated dye.

These results show that the predicted vignetting distance is an overestimate of what was measured. For the uniform light source the predicted and measured values were off by a factor ranging from about 1.1 to 1.9 with an average error of a factor of about 1.58. PLIF-illuminated images exhibit a larger error factor ranging from about 3.2 to 4.0 with an average of about 3.6.

4.1.3. Vignetting Conclusions

The goal of this preliminary experiment was to demonstrate that vignetting will have a significant effect on the accuracy of light intensity measurements of formaldehyde concentration images when light is viewed across an obstruction of significant depth. It was also intended to show a direct relationship between obstruction depth and vignetting distance. Obstructions of 12.7, 38.1, 63.5, and 88.9 mm were placed in front of the light source and images were taken to measure the effects of vignetting. These obstructions bracketed all possible obstruction depths that could be imposed by engine components. With an approximately uniform light source, results showed that as increases were made in the depth of the obstruction, vignetting became more prominent at the obstruction surface and effects extended further off of the obstruction boundary. However, predictions were high by a factor between 1.1 and 1.9 with an average factor of 1.58. To more accurately represent the condition in an optical engine, a PLIF-illuminated light source was used and blocked by a combination of razorblade and the same variable-depth obstruction. Results were similar in that vignetting amplitude and distance increased with an increase in obstruction depth: however, in the PLIF-imaged setup the measured values were even lower. Factors of error ranged from 3.2 to 4.0 with an average of 3.6. A reason for the low measured values may be a result of the effect being too faint for the camera to perceive at its dimmest location. Predictions are accurate for measuring trends are consistent if augmented with a factor of adjustment.

Two unexpected results were the amount of light present over the obstructed field of view as well as excess light over the unobstructed portion causing relative light intensity to both fade gradually to zero and rise above 1.0. This light can be attributed to reflection off of

the top of the boundary. Light reflecting off of that surface would be visible to one half of the lens and could contribute to an overall increase in the light absorbed by the camera.

In a combustion chamber with an accessible height of only 14 mm and a viewable clearance distance of only 3.3 mm at TDC, the vignetting distances measured in this experiment occupy a significant portion or all of the imaged cross-sectional area. Since most images will be taken as the piston approaches its TDC position this effect could prevent accurate measurement of formaldehyde concentrations from being made.

The solution developed for this is to access the engine with the laser and camera through the same optical access spacer ring window. This requires the laser to enter the combustion chamber at an angle. This significantly decreases the obstruction depth to a distance just larger than the spacer ring thickness or about 21 mm. However, two other problems arise because of this arrangement. Flare will be an issue since the laser is entering through the window that is being viewed by the camera. Depth of field will also be a concern since the camera is no longer normal to the laser sheet.

4.2. Flare

Figure 4.16 is an enlarged diagram of the laser sheet entering the combustion chamber through the access window. The camera is located at the bottom of the figure. The flare sources are the result of light scattering when it passes from one optical medium to the next. In this experiment, flare occurs at both surfaces of the spacer ring window as it enters the combustion chamber. The flare off of the inner window surface is located at the position of interest, i.e. the near-wall region, and if unchecked, the high signal from the flare could overwhelm the formaldehyde signal.

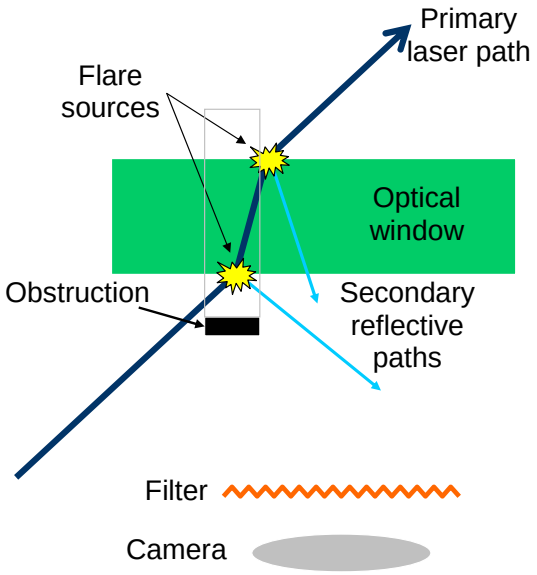

Figure 4.16 Enlarged view of the laser sheet passing through the access window with resulting flare and methods for removing flare (obstruction & filter).

For the outer flare source, an obstruction that blocks the path of the light to the camera, but not the path of the laser to the window surface was used. This method is sufficient for the external surface flare because it is far enough removed laterally from the region of interest (ROI). A suitable size obstruction can be made that is wider than the flare and narrow enough to allow the laser to pass behind it to the engine and avoid obstructing any part of the ROI. Since the internal surface flare is immediately adjacent to the ROI as well as inside the engine, no simple obstruction can be used. For this flare, a filter was employed to block the wavelength of the laser light flare while still allowing the fluorescence wavelength to pass. Formaldehyde absorbs light at a wavelength of 355 nm, but fluoresces at a range of 400-550 nm. Therefore, a filter that blocks light at 355 nm while allowing light at 400-550 nm to pass would work to suppress any flare at the internal surface. A pair of filters were used to block the flare from the sheet of 355 nm light, the extraneous room light, and residual 532 nm light

that was not completely dumped. The filters used were a GG-400 high-pass filter that blocked light below a wavelength of about 400 nm and a low-pass 505FD64-50S filter that suppresses light with wavelengths above 500 nm. Both filters have transmission values around 90% at the fluorescing wavelengths. A total intensity reduction of around 80% is seen from the filter pair for a combined band pass filter effective from 400 to 500 nm. Figures 4.17 and 4.18 show the transmission plots of the two filters as a function of wavelength.

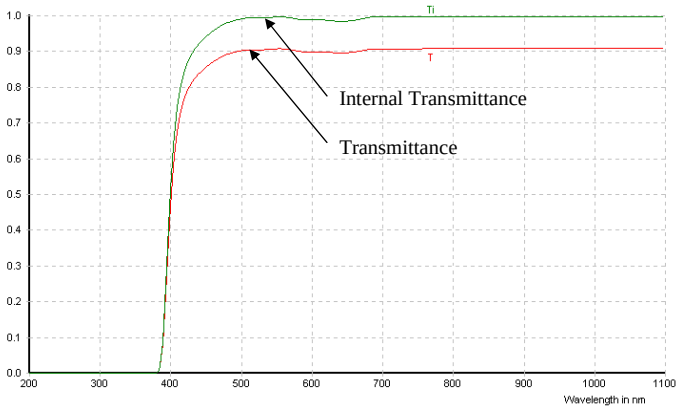

Figure 4.17 Transmittance plot for GG-400 high pass filter [30].

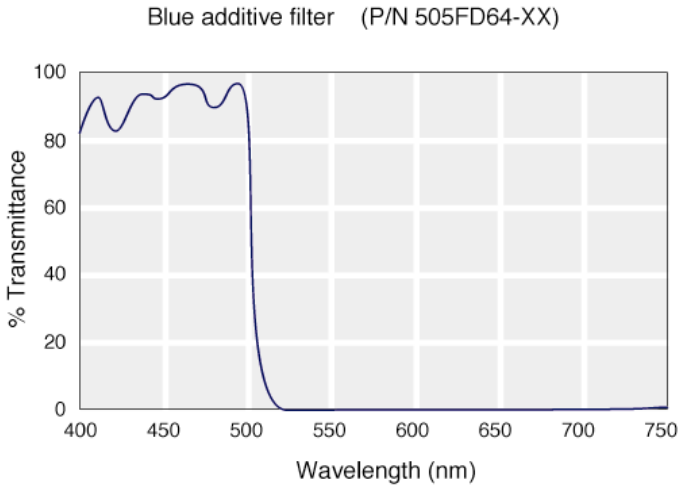

Figure 4.18 Transmittance plot for 505FD64-50S low pass filter [31].

4.3. Depth of Field

Finally, depth of field becomes an issue since the laser path through the engine is not perpendicular to the camera. Depth of field is a measure of the maximum distance away from the focal plane where the image is still considered to be sufficiently resolved. It can be thought of as a rate at which focus is lost as an object is moved away from the focal plane/the distance between the nearest and farthest objects that are still in focus. Retained focus at a greater distance from the focal plane corresponds to a greater depth of field. Since the distance from the camera lens to the illuminated combustion is increasing as the laser propagates from left to right into the engine, a lateral pixel distance is directly related to the imaged depth into the engine by the angle at which the laser enters the combustion chamber.

When attempting to resolve an image with varying depth, focus is critical. Therefore, a depth of field of at least 10 mm was desired in order to obtain significant resolution. Optical characteristics including focal length, aperture, and object distance allow for manipulating the depth of field. Depth of field can be increased by using a shorter focal length lens, decreasing the size of the aperture, or increasing the object distance. There are drawbacks to each of these remedies. A shorter focal length lens at the same object distance yields a wider view and thus a smaller image and reduced resolution. Reducing the aperture decreases the amount of light available to the camera in an already low light environment. A smaller aperture would in effect lower the signal to noise ratio of the camera. Increasing the object distance again decreases the image size and lowers resolution. With these considerations a Nikon 85 mm focal length lens with a 12 mm extension tube was chosen using the largest aperture setting of f/1.4. At a distance of 230 mm from the focal plane 5

mm inside of the combustion chamber surface to the front of the camera lens more than 10 mm depth of field was achieved. Magnification was 0.42 giving a resolution of 57 μm/pixel.

Complicating this issue is the limited area through which to view the combustion fluorescence in the engine. The window allows a viewable area of only 300 mm^2. When the piston is near TDC, as it was for the images taken in this project, the area can be reduced to just over 56 mm^2. A laser passing through this same window also decreases the available imaging size. Since the laser impinges upon the window at an angle, the cross-sectional area available for imaging exists only where laser light crosses the field of view after it has passed through the window and is traversing the combustion chamber. This area is dependent on the angle at which the light hits the window and at what point across the window the light impinges. Figure 4.19 depicts the laser path entering the engine through the access window.

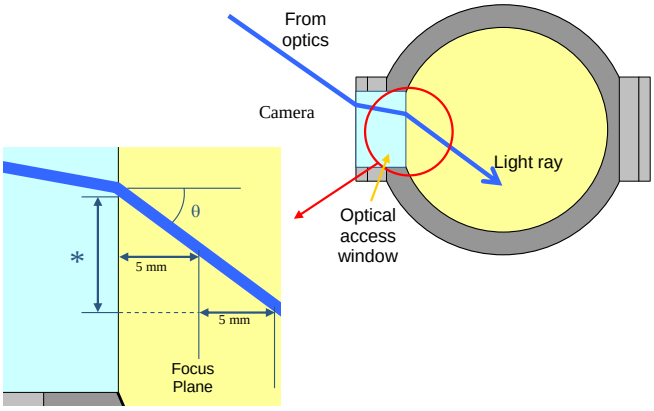

Figure 4.19 Diagram of laser sheet entering combustion chamber through access window with depth of field considerations.

A compromise must be made to determine the optimum angle of incidence for the laser. An angle close to perpendicular to the window surface is considered steep or small. A steeper incident angle means light will travel deeper into the combustion chamber faster

relative to its propagation perpendicular to the camera. A shallow or large angle is an angle that produces an in-cylinder sheet closer to parallel with the window surface. Steeper incident angles require a greater depth of field from the camera. As the incident angle increases, depth of field requirements relax. However, this means the laser does not enter the combustion chamber until further across the optical access window surface, thus decreasing the field of view. Figure 4.20 is a flow chart of the consequences of incident angle choice.

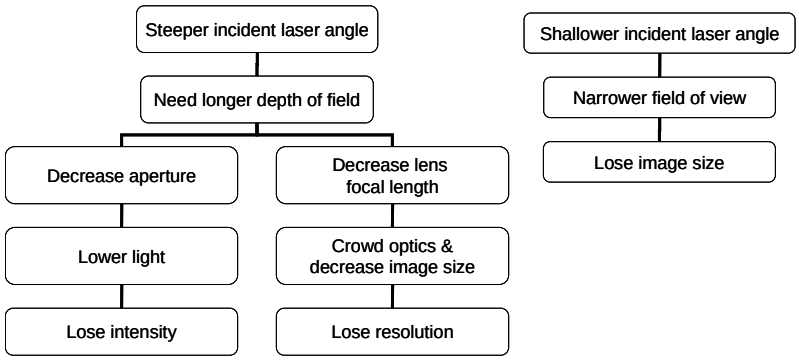

Figure 4.20 Flow chart of consequences for incident angle calculations.

The angle was measured using a two-level block with a known step height. The block was placed in the beam path and images were taken to record the reflections off of the two offset surfaces. The peak levels of flare were pinpointed, and the distance between them across the camera's field of view was measured. Along with the know step height the angle of propagation through the combustion chamber could be calculated. Figure 4.21 diagrams this calculation.

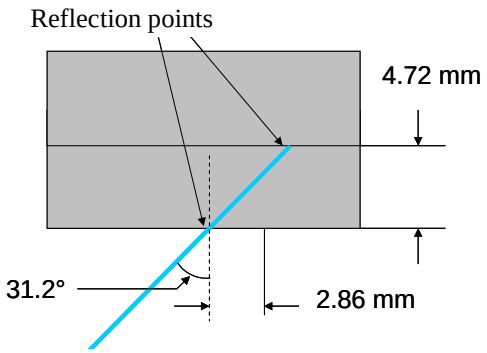

Figure 4.21 Diagram of method for calculating the laser sheet incident angle.

5. Near-wall Imaging of Formaldehyde in an HCCI Engine

5.1. Image Orientation

Before discussing in detail the results of this experiment, it is important to become familiar with interpreting the data images. The illuminated field of view in all images is of the upper right portion of the optical access window in the engine spacer ring. This area represents the portion of the combustion chamber volume above the piston that is illuminated by the laser after it passes through the window. The entire CCD camera area is a 512 x 512 pixel grid, but only a 176 x 98 pixel portion of that was recorded by the software for most data sets. Working with a smaller recorded area speeds up image acquisition time, which allows data to be taken in a shorter period of time, minimizing the effects of transients associated with thermal system changes. Moving across the ROI from left to right progresses deeper into the combustion chamber according to the relationship established by the 31.2° incident angle of the laser. A sample set of images can be found in Figure 5.1.

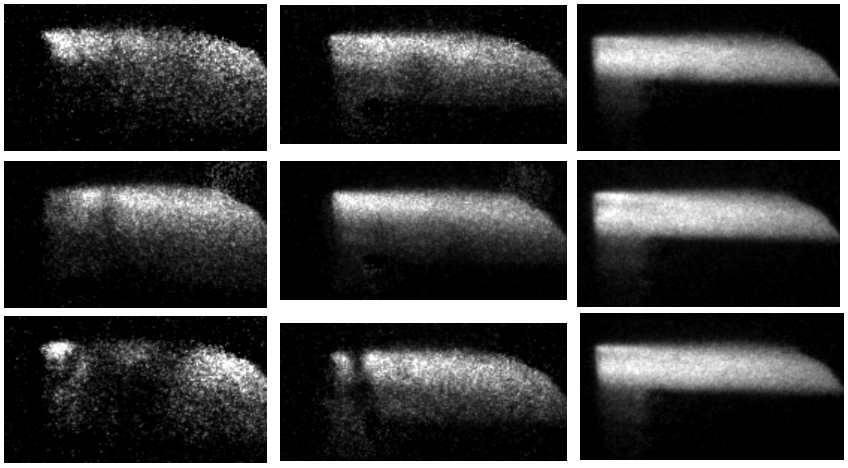

Figure 5.1 Sample data images of PLIF illuminated formaldehyde.

In these images, brighter areas represent regions of higher formaldehyde concentration. No precise quantitative measurements were attempted, but changes in intensity along the beam path are expected to represent linear changes in intensity.

Figures 5.2 and 5.3 illustrate two views of the illuminated field in relationship to the critical engine components. Figure 5.2 looks vertically down the bore axis. This view makes clear the relationship between the horizontal image dimension and the associated depth into the combustion chamber. Also highlighted here is the location of flare at the window surface.

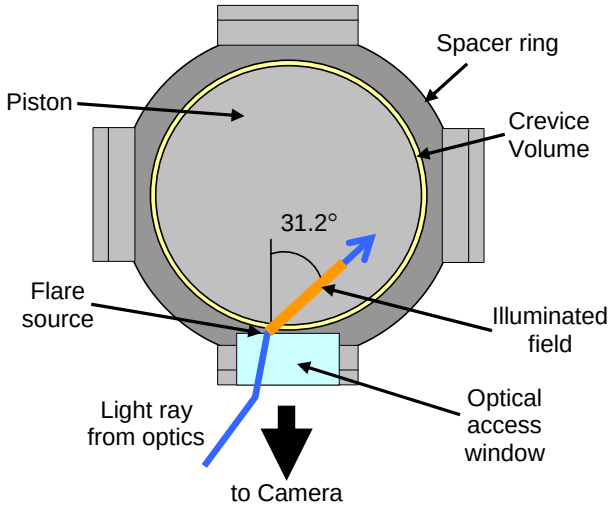

Figure 5.2 Top view of engine spacer ring assembly, piston, and laser path.

Figure 5.3 shows the camera's view of the imaged area. Visible in this view are the edge of the window retainer, the piston, and the location at which the laser enters the combustion chamber. At the far left of the inset image in Figure 5.3, where the fluorescence signal begins, is the location at which the laser enters the combustion chamber. The dark rectangular area in the bottom-right corner is the area blocked by the piston. Immediately to the left of the piston is formaldehyde illuminated in the crevice volume.

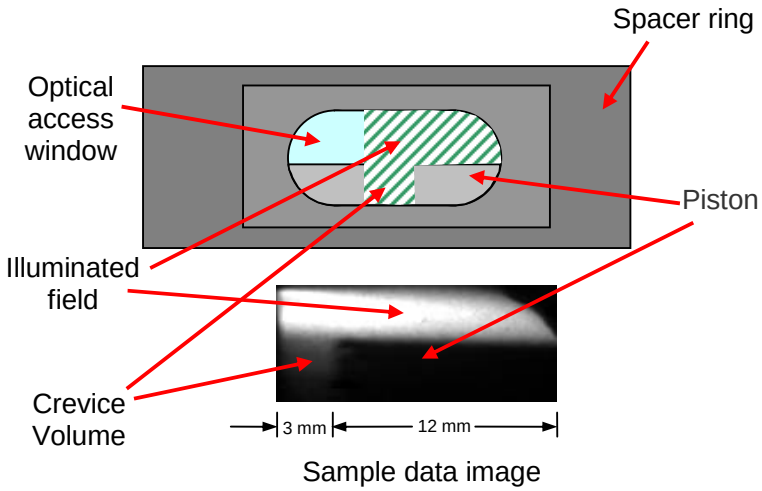

Figure 5.3 Front view of engine spacer ring assembly, piston, and laser illuminated field.

This engine has a relatively large crevice volume for two reasons. First, larger piston-bore clearances are required due to the tendency of the long piston in an optical engine to experience larger degrees of tilt during operation. Second, referring to Figure 5.2, it can be seen that the inner surface of the window is not flush with the bore surface. Instead, there is an additional gap between the window and the bore of about 2 mm. The resulting gap between the piston and window surfaces is just over 3 mm.

5.2. Sample Data and Correction

Images were taken in sets of 50 for both the background and fired data images. The background data were averaged to minimize any pulse-to-pulse variations of the laser and camera noise. To investigate the general nature of the combustion, the corrected images were averaged. Corrected images were obtained by subtracting the averaged background image from the average data image. Individual corrected images were also investigated to show the combustion characteristics for a single cycle that are lost in the averaging process.

Figures 5.4a and 5.4b respectively, show averaged background and corrected fired data images taken at 10° bTDC for operation at an equivalence ratio of 0.26 for the fired case. For these averaged images, intensity profiles were taken horizontally from the inner window surface to up to 2.5 mm across the window (4 mm off the bore) for the height of the fluid not blocked or affected by the piston. Figures 5.4a and 5.4b show this area with a box.

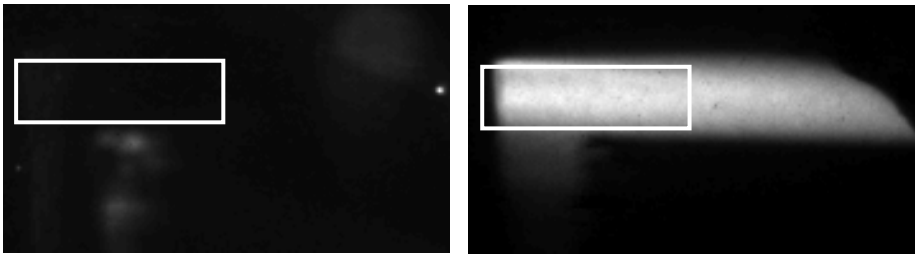

a b

Figure 5.4 Averaged background (a) and corrected data (b) images for 8 mg of fuel per cycle at 10° bTDC.

Image correction artifacts are present in some of the data presented here and merit an explanation due to their effect on the data in potentially critical areas. 'Holes' appear in some of the data images such as in Figures 5.5c and 5.6c. The holes are the result of over-subtraction in the post-processing image math. These occur when an area is brighter in the background image than in the fired data image or if the difference in intensity between the data and background image is much smaller than the overall image intensity difference. Over-subtraction results from flare off of the inner window surface or the line where the laser hits the piston surface or variation in the laser pulse power. After extended periods of firing, the window and piston can become fouled with deposits that fluoresce when hit with the laser sheet. Figures 5.5 and 5.6 are examples of high amounts of flare in these two areas.

In the case of piston flare interference in Figure 5.5, the only adverse effect is a reduced height above the piston over which to average horizontal intensity profiles. In the background image the peak intensity at the bright spot reaches a level of over 54,000 (out of 65,536) while at the same pixel in the fired case the value is only about 34,000. Since the imaging software does not deal with negative intensities, when subtracted, this results in a local intensity of zero.

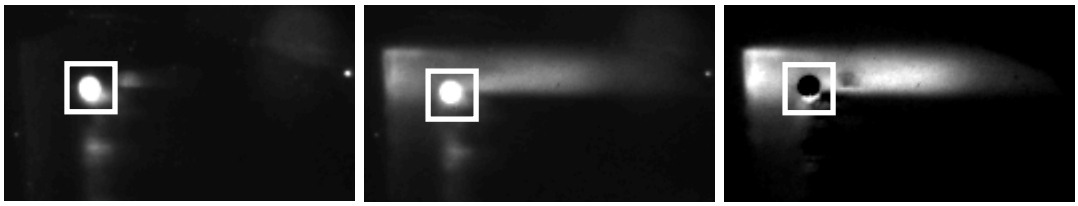

a b c

Figure 5.5 Piston flare visible in averaged background (a), individual fired (b), and averaged corrected (c) data images.

In Figure 5.6, window flare is the cause of the highlighted region. While the intensity for this region is not greater in the background image than in the data image, the ratio of data image intensity to background image intensity is far smaller for the corrupted area than it is for the rest of the picture. Low relative intensity is the cause of this blank spot in the data.

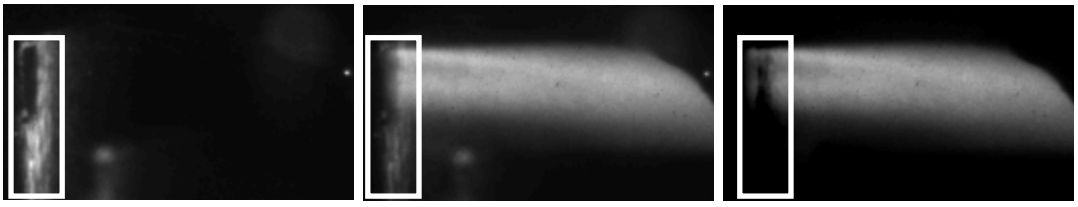

a b c

Figure 5.6 Window flare visible in averaged background (a), individual fired (b), and averaged corrected (c) data images.

Quantitatively this can be seen in Figure 5.7. The image on the left represents the ratio of intensity of the data image to the background image. The plot on the right is a display of relative intensity along the horizontal line in the image.

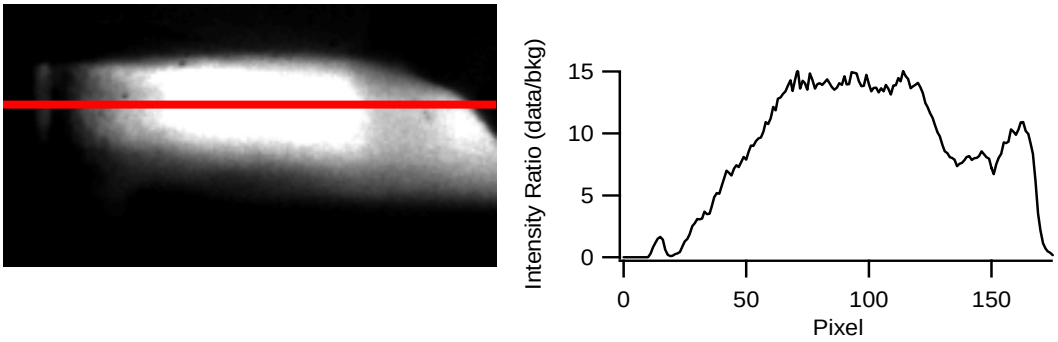

Figure 5.7 Image of the ratio of data image intensity to background image intensity and intensity profile for the line indicated on the image.

While most of the data image has an intensity of around ten to fifteen times that of the background image, the corrupted area that was visible in Figure 5.6 shows an intensity ratio of less than five. In the corrected image, therefore, this area shows up very dim. The region of the image affected in this data set is the critical area immediately against the window surface where boundary layer measurements are attempting to be made. Because of the loss of data near the window surface, this data set was discarded.

The individual background images can give us an idea of how stable the conditions in the motoring engine are before firing takes place. If there are large inconsistencies in the laser power from pulse to pulse we can see large fluctuations in the intensity of these images. Timing problems would be apparent with varying piston heights. Figure 5.8 is a subset of the fifty individual background images taken at 17° bTDC. These images show a sufficiently stable motoring environment. The tall stripe of light at the far left of the image is the flare

generated by the laser sheet passing from the window into the combustion chamber. The shorter illuminated area to the right is flare off of the piston surface. As discussed, excessive flare in these areas can have a significant effect on the final data image depending on its intensity.

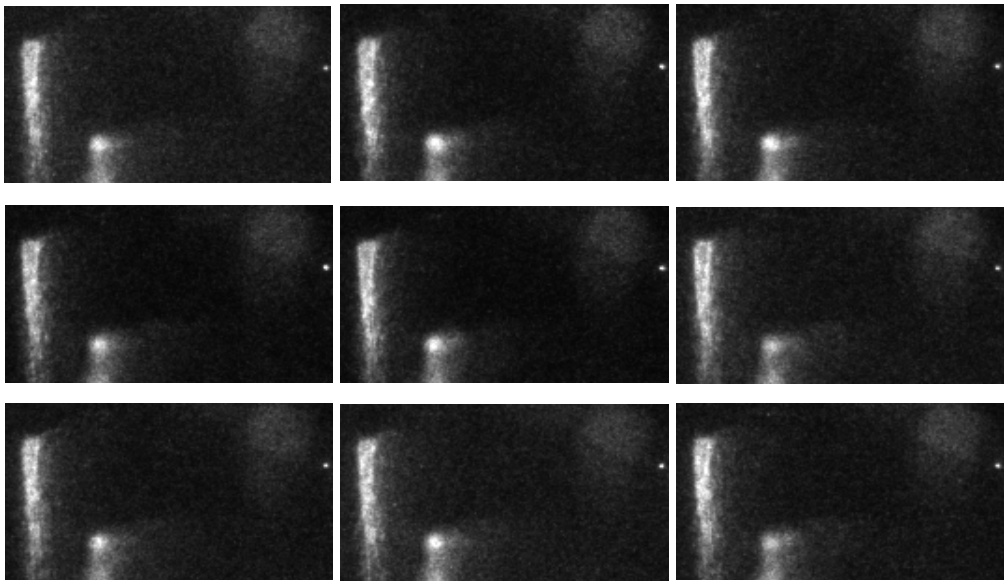

Figure 5.8 Sample of background images taken at 17° bTDC. Visible is piston and window flare.

Similarly, individual data images are important to view the stability and consistency of the cycle-to-cycle combustion. While the averaged images display important information about general trends in formaldehyde concentration and the global significance of the boundary layer effect, individual images are important when observing actual physical conditions in the engine for a single cycle. This data describes the structure of the reacting fluid and can lend weight to observed trends in the averaged images. Figure 5.9 is a set of raw, individual cycle data images taken at 20° bTDC and a fueling rate of 7 mg injected per cycle (Φ=0.23). These images show the presence of formaldehyde in varying distributions

through the combustion chamber. The individual data and background images will give an important indication as to the cycle-by-cycle structure and spatial concentration gradients present during individual combustion events.

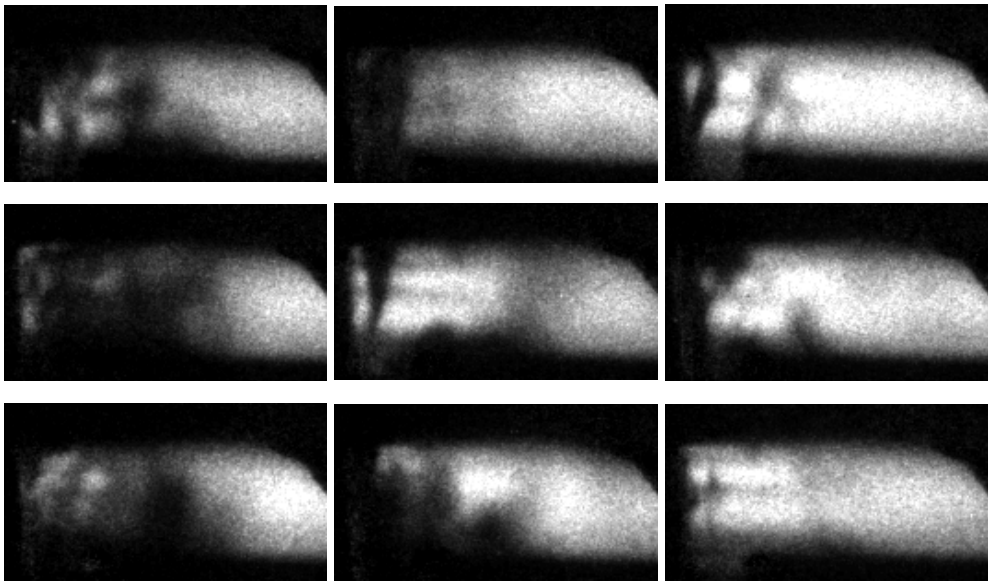

Figure 5.9 Sample of individual fired images taken at 20° bTDC with 7 mg fueling.

Corrupted data sets are an unavoidable aspect of optical engine data acquisition. While firing the engine, deposits appear on the inner window surface and piston, contributing to a large amount of flare in some images that is then incorporated into the corrected data. After all of the data were acquired and processed, it was sorted by hand so that further analysis could be concentrated on those sets with minimal levels of signal interference.

5.3. Spatial Resolution

At the far left of the visible fluorescence signal in the data images, where the laser enters the combustion chamber, is a critical area for accurate intensity gradient measurements to be made. It must be determined, therefore, how the spatial resolution of the data images

compares with the highest achievable resolution given the imaging environment. One limitation to the resolution of these images is the non-orthogonal relationship between the laser path and the camera's line of sight. There will be one distance along the laser path that will be in the focal plane. All other data points are removed some distance and, as a result, have decreased spatial resolution. Another source of image blurring is the camera itself. Intensified cameras generally have lower spatial resolution due to the intensifier, sacrificing image clarity for signal strength and a high signal to noise ratio.

5.3.1. Qualification

A short series of images were taken of Bucky Badger through the engine access window at distances away from the inner surface that illustrate the loss of spatial resolution with an increased distance off of the focal plane. These images were taken under identical camera settings as the formaldehyde PLIF images. Figure 5.10 is a set of three images taken at 1, 3, 6, and 8 mm away from the inner window surface. The focal plane for these images appears to be closest to 3 mm away from the window since this image is clearest.

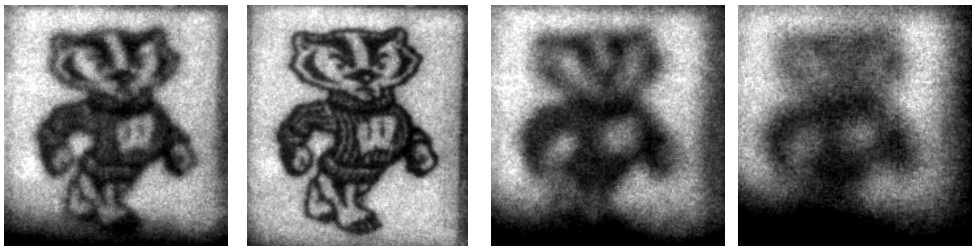

Figure 5.10 Images of Bucky Badger showing relative focus at a range of distances from the inner window surface. Left to Right: 1, 3, 6, 8 mm.

A more quantitative measurement was made of the spatial resolution achievable at the window surface. Black optical tape was placed on the inner surface of the window and the region was back-illuminated. Images were taken and averaged to mimic the imaging method used for data acquisition. Figure 5.11 is an average image of 50 exposures of the taped window and an associated line profile.

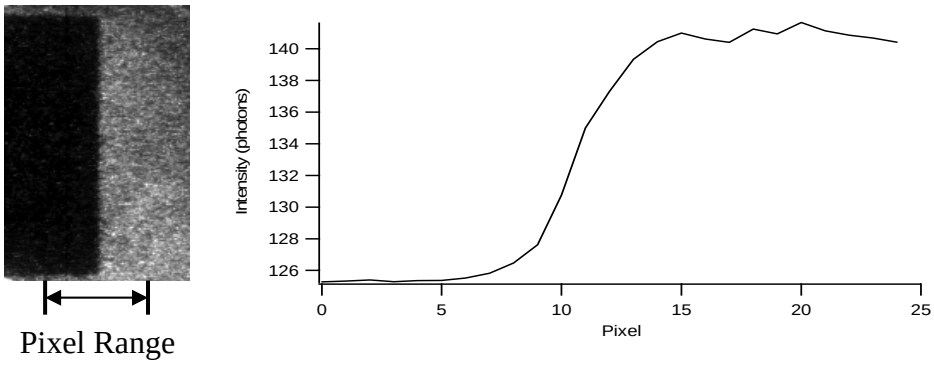

Figure 5.11 Quantification of spatial resolution at the inner window surface.

The tape provided a clean line that, when imaged and analyzed would show the spatial resolution limitations of the camera and give a base for comparison with the initial intensity slope of the PLIF data images. An averaged horizontal line profile was found for the height of the tape across the edge of the tape. The plot in Figure 5.11 shows that the step change in intensity occurs over a range of about 5-6 pixels. Therefore, a resolution of 5-6 pixels or 0.31 mm across the image is the best we can expect from the data. Considering the 31.2° incident angle, the resolution off of the window surface is about 0.5 mm.

5.3.2. Image Data

Figure 5.12 shows a typical set of data images consisting of an averaged background, averaged corrected data, and two random individual exposures from the data set taken at 10 bTDC at an equivalence ratio of 0.26. A line profile of each image was taken at the same height, located by the arrows, to demonstrate the pixel range over which the image intensity rises from a transitions from low to high.

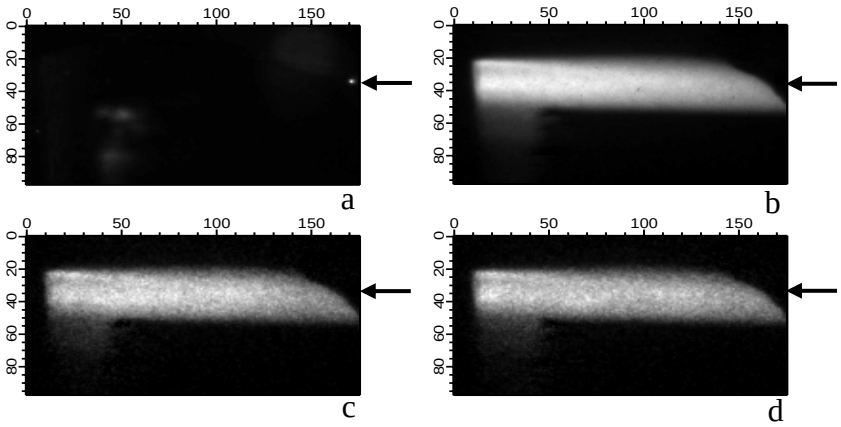

Figure 5.12 Images of averaged background (a), averaged fired (b), and two individual fired cycles (c&d) with indicated height of intensity profile.

Figure 5.13 is a plot of the four generated line profiles scaled to show depth from the inner window surface. When compared with the line profile from the tape image, the pixel ranges for the intensity transitions are approximately equal. In all three data image line profiles that have a formaldehyde signal, the intensity rises from a base level to an average high within 6 pixels or 0.57 mm. Therefore, we can conclude that, despite the flare at the critical area near the inner window surface, spatial resolution is only limited by the camera.

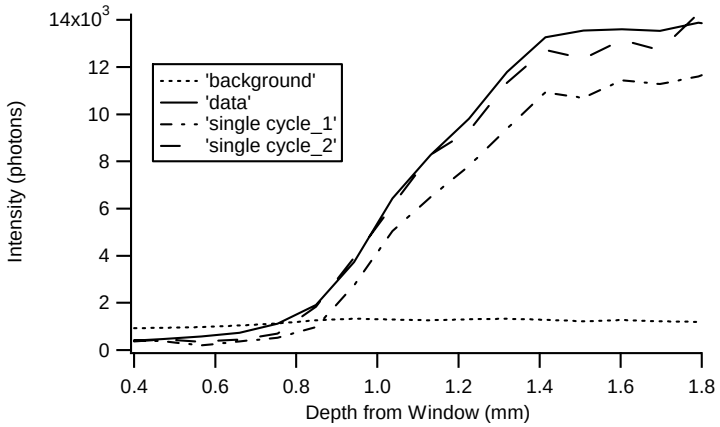

Figure 5.13 Intensity profile for the four images in Figure 5.12.

5.4. Timing Sweep

The data were sorted after acquisition and organized by image timing and mass of fuel injected per cycle. The first set of data presented consists of images from six different crank angle positions for a fueling rate of 8 mg per cycle (Φ=0.26). The images were taken at 23, 15, 10, 6, 5, and 2 CAD bTDC. Figure 5.14 is a sample plot of the heat release rate, motored, and fired pressure traces; the vertical lines indicate the image timings. The heat release and pressure plots are samples, and therefore, not precisely applicable to all image sets shown here. Fluctuations exist in the timing and intensity of the heat release between data sets relative to the image timing. It should be noted that at this equivalence ratio, both stages of the characteristic two-stage heat release exist. The points of most interest are located around the first and second heat release events. In the subsequent discussions, only data with minimal flare from window and piston fouling are presented.

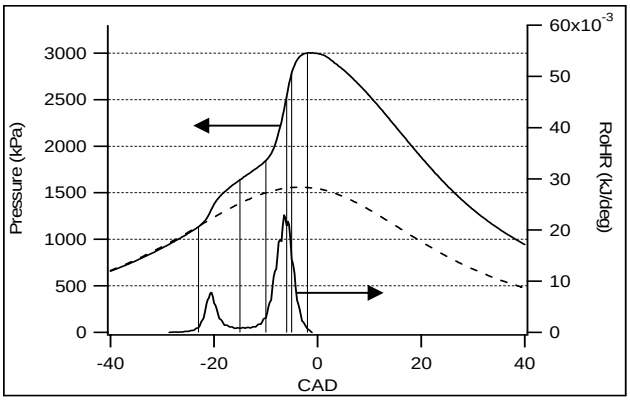

Figure 5.14 Pressure (motored and fired) and heat release curves at 8 mg fueling for timing sweep data. Vertical lines are image timings (23, 15, 10, 6, 5, and 2° bTDC.

5.4.1. Averaged Images

Figure 5.15 shows the averaged corrected images for the six timings at this equivalence ratio. At 23° bTDC the first heat release stage has just begun for this data set, and as expected, there is a very low formaldehyde signal since combustion reactions have not yet progressed far enough for its formation. In the images taken at 15° bTDC, the beginning of a significant formaldehyde concentration is seen coinciding with the delay between heat releases. Initial formation appears to be fairly uniform across the image which is inconsistent with the consequences of a theory for significant boundary layer cooling or quenching effects. By 10° bTDC the formaldehyde concentration has peaked within this data, and a strong signal is seen all the way to the window surface. During the second stage heat release, at 6 and 5° bTDC, the formaldehyde signal level begins to decrease, indicating the beginning of consumption. Finally at 2° bTDC, the formaldehyde has been mostly consumed.

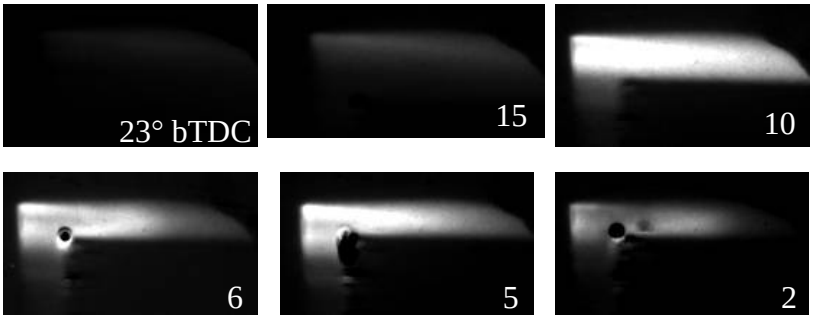

Figure 5.15 Average corrected fired data images for the timings indicated at a fueling rate of 8 mg/cycle.

5.4.2. Image Profiles

Intensity profiles for the average images of Figure 5.15 are displayed in Figure 5.16. Zero depth into the chamber was determined by the point of steepest slope. These plots show the averaged intensity profile for a height of 4 mm corresponding to the box covering the height of the unobstructed field as described in Figure 5.4. Intensity is quantified on the vertical axis of these plots. Maximum intensities indicate agreement with the expected trend of formation and consumption coinciding with the first and second stages of heat release respectively. At 23° bTDC the intensity is very low; however, there is a distinctly more gradual slope to the curve than the others. This may suggest that the formation of formaldehyde is slightly slower near the combustion chamber surfaces early in the combustion process, before any significant heat release takes place. At 15° bTDC this effect is still present but to a smaller degree. During the second stage heat release, plots for 10, 6, and 5° bTDC are characterized by very steep initial slopes and flat profiles extending past 3 mm from the window surface. Steep intensity slopes followed by relatively flat curves signify a uniform concentration of formaldehyde throughout the imaged area.

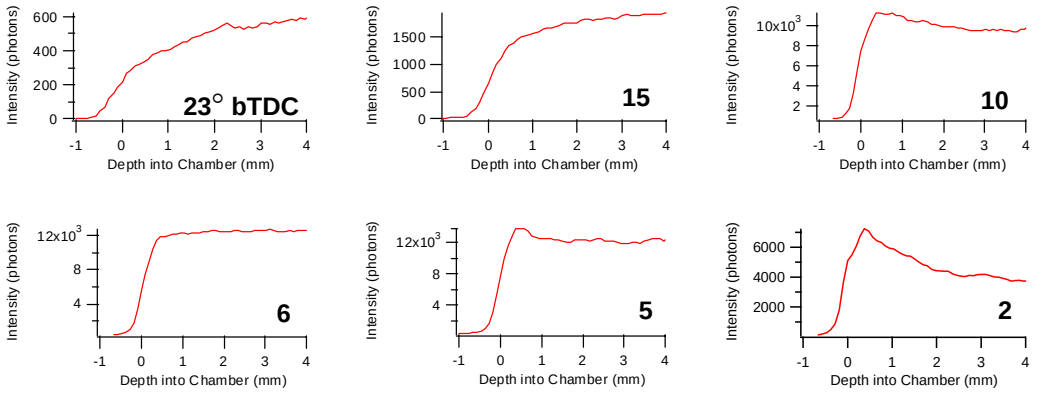

Figure 5.16 Averaged intensity profiles at the window surface for the timings indicated at 8 mg/cycle fueling.

The pixel intensity across these slopes rises from zero to a maximum over a distance of less than 0.25 mm from the window surface; corresponding to about 3 pixels. Considering the achievable resolution of the camera is approximately 6 pixels or 0.6 mm into the combustion chamber, we can conclude that our image is sufficiently resolved at the window surface for precise intensity measurements. Near the completion of the second stage heat release, at 2° bTDC, the signal reaches a peak less than 0.25 mm away from the wall, followed by a 35% decline in intensity. Formaldehyde appears to be consumed more slowly at the very edge of the chamber volume. This thickness against the chamber wall is estimated at less than 0.5 mm.

5.4.3. Individual Cycle Data

As mentioned before, individual cycle images are useful as supplementary data for observed trends in the averaged images. Figure 5.17 is a random sample of images for each of the six timings just described. The grayscale is equal throughout each column of images,

but different between columns to show contrast and detail available in each set of images. Relative grayscale magnifications are indicated below each column.

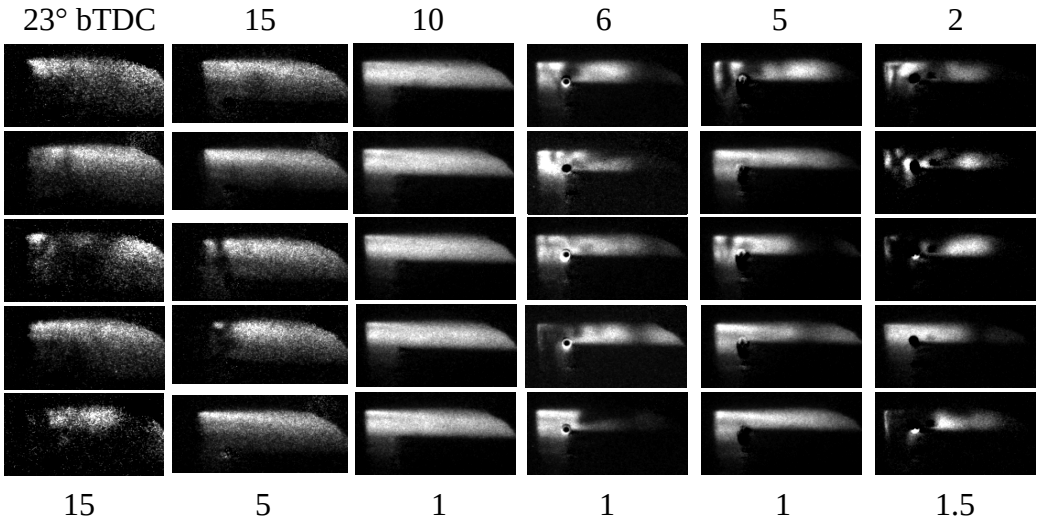

Figure 5.17 Random images from each image timing (indicated top). Image intensity is scaled to show detail (relative scale indicated bottom).

Consider the images acquired at 23° bTDC. The data in Figure 5.16 suggested a significant boundary layer existed with reduced formaldehyde formation due to cooler temperatures near the wall. However, several of the images in the small selection of Figure 5.17 at the same timing show significant amounts of formaldehyde right up against the window. In addition there seems to be no preferred location for the formaldehyde to initially form. Figure 5.18 shows line profiles for the averaged corrected data image acquired at 23° bTDC and two of the individual cycle corrected data images. Although the average image shows a more gradual formaldehyde concentration profile, the individual shots reveal that high levels of concentration can form directly at the window surface.

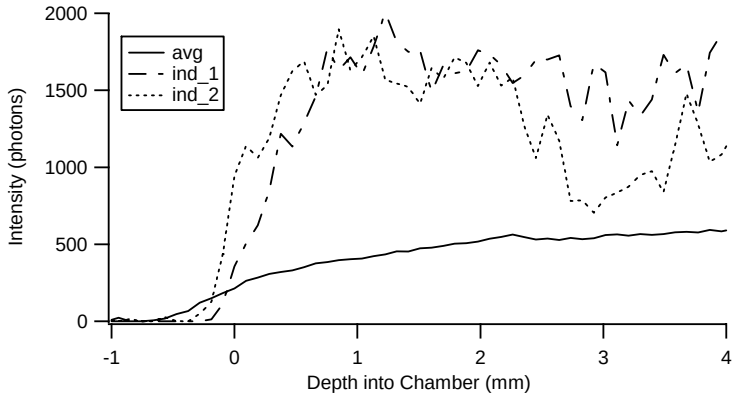

Figure 5.18 Intensity profile for average corrected fired image and two individual cycle images for 8 mg/cycle fueling, acquired at 23° bTDC.

With the completion of the first heat release stage and the onset of the second, concentration becomes more uniform even within a single cycle. During the second stage of heat release, a heterogeneous structure is again seen with no apparent preference for the locations of the formaldehyde to first be consumed. In some images formaldehyde persists at least 10 mm into the combustion chamber, while in other cycles, it has been consumed intermittently across the field of view. At 2° bTDC there is still no preferred location for the formaldehyde consumption. The only consistent feature of images taken after the second heat release stage is the low signal at the right of the image or the deepest view into the combustion chamber. Figure 5.19 shows line profiles for the averaged corrected data image and two individual corrected data images for the set acquired at 2° bTDC. While the averaged intensity profile shows an initial intensity peak followed by a sharp drop at about 0.5 mm away from the wall, individual cycle images illustrate a steady, or even rising, intensity profile moving deeper into the combustion chamber. With a significant boundary layer effect, formaldehyde should have consistently persisted up against the window surface

late into the cycle. Many of the images; however, indicate locally low concentrations near the wall.

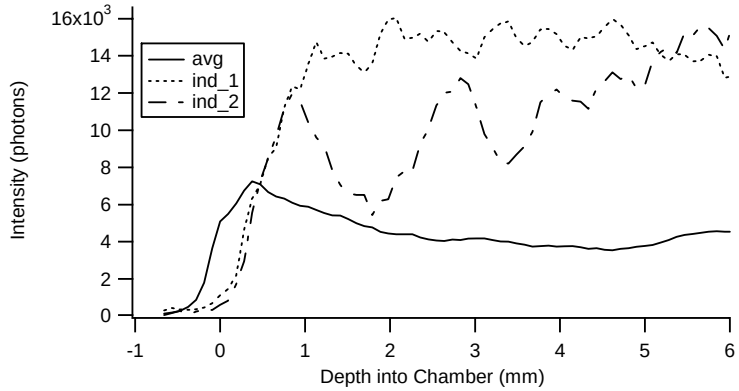

Figure 5.19 Intensity profile for average corrected fired image and two individual cycle images for 8 mg/cycle fueling, acquired at 2° bTDC.

As partial verification that the fluorescence signal was representative of formaldehyde concentration and not some other species, image data was taken later in the cycle to observe the signal strength where formaldehyde should be completely consumed. Figure 5.20 shows an averaged background and corrected data image taken at TDC with a fueling rate of 8 mg per cycle (Φ=0.26). At this crank angle the fluorescence signal is no higher than the noise floor of the image, save a spot of background flare.

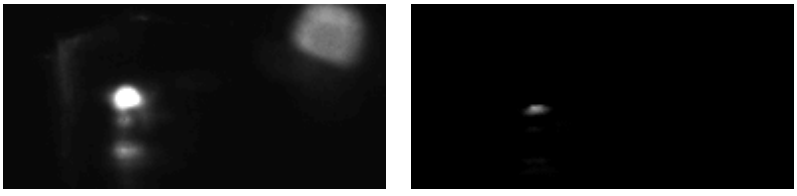

a b

Figure 5.20 Average background (a) and corrected fired (b) data images for fueling of 8 mg/cycle taken at TDC.

5.5. Fuel Sweep

The second set of data has been organized into a fueling, or equivalence ratio, sweep with images taken at approximately the same crank angle position. Fueling rates of 2, 7, and 8 mg per cycle (Φ=0.06, 0.23, 0.26) were imaged at 10° bTDC and fueling of 5 mg per cycle (Φ=0.16) was recorded at 12° bTDC. Figure 5.21 is a plot of heat release and fired pressure curves for all four conditions in the data set. A sample motored curve is also included.

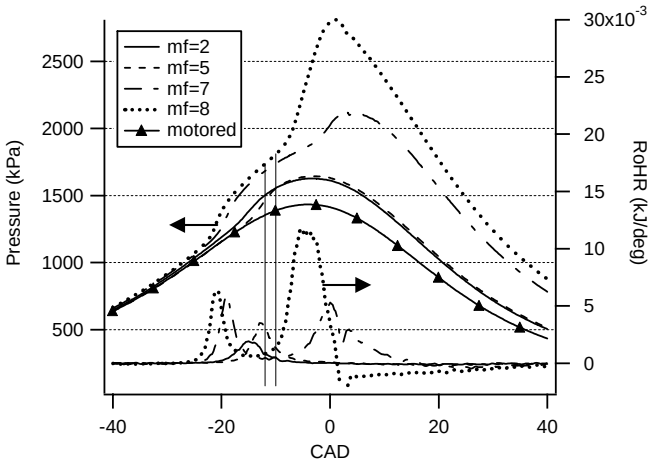

Figure 5.21 Pressure and heat release curves for fueling rates of 2, 5, 7, and 8 mg/cycle. Vertical lines indicate image timings (10 and 12° bTDC).

It is important to notice, when considering formaldehyde consumption, that two-stage heat release only occurs for the two richer equivalence ratios. For this data set, the image timing of 10-12° bTDC occurred between the two heat release stages for the richer cases and during or toward the end of the first stage for the leaner operating conditions. The locations of these images in relationship to the heat release are, again, indicated by vertical lines in Figure 5.21.

5.5.1. Averaged Images

The averaged corrected data images for the four conditions are shown in Figure 5.22. As the equivalence ratio is increased, the intensity of the formaldehyde signal also increases. An increase in formaldehyde concentration with fueling rate is consistent with the expected trend and models.

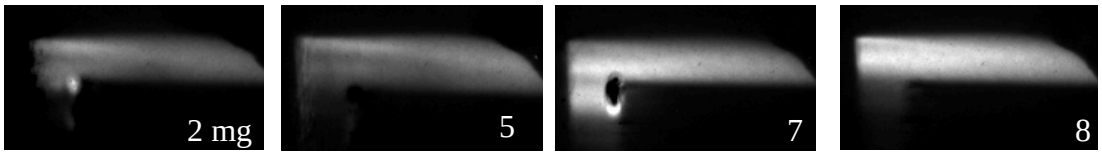

Figure 5.22 Average corrected fired data images for the fueling rates indicated at timings of 10 and 12° bTDC.

It also appears from these images that the mean formaldehyde concentration is relatively uniform across the field of view for all equivalence ratios. Uniform concentration up to the wall is also consistent with what was seen in the previous timing sweep data set at 10° bTDC, but again, counter to model predictions. There seems to be no significant boundary layer effect on the formaldehyde concentration at any of these equivalence ratios at this crank timing. In the leanest operating condition, formaldehyde was observed up to 20° aTDC, see Figure 5.23, consistent with the finding of Kim and Ghandhi.

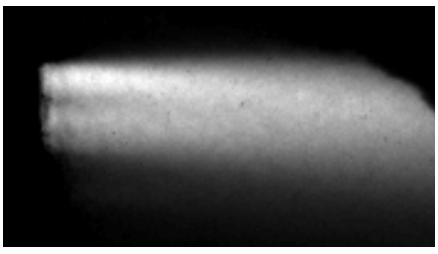

Figure 5.23 Formaldehyde signal present at 20° aTDC for a fueling rate of 2 mg/cycle.

5.5.2. Intensity Profiles

Figure 5.24 shows the intensity profile plots for the mean images from the fueling sweep. In these plots, a height of 4 mm is employed as described in Figure 5.4.

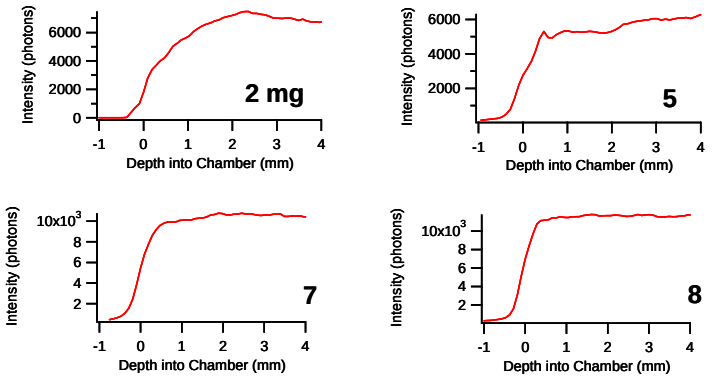

Figure 5.24 Averaged intensity profiles at the window surface for the fueling rates indicated at 10 and 12° bTDC.

Quantitatively, these plots show an increase in intensity with higher equivalence ratios. At 2 and 5 mg of fuel per cycle there is not a significant difference in the overall image intensity. Since the fired pressure traces and the heat release curves for these two cases are also very similar in magnitude, it is not surprising that formaldehyde concentration should be fairly similar. For fueling of 5, 7, and 8 mg per cycle, the pixel intensity across the initial slopes rises from zero to a maximum over a distance of about 0.3 to 0.4 mm from the window surface about 3-4 pixels. The intensity profile for the leanest operating condition shows a much more gradual slope to a maximum. This is the result of a corrupted section of the image due to background flare off of the window, see Figure 5.6. With an achievable camera resolution of approximately 6 pixels or 0.6 mm into the combustion chamber, the data images indicate that again, the spatial resolution of the image is only limited by the camera, discounting the leanest case. For the 2 mg per cycle case, intensity remains near zero for

about 1 mm next to the chamber wall. Zero intensity here results from over-subtraction of background flare. All other data for this equivalence ratio near this crank timing have a larger affected area.

5.5.3. Individual Cycle Data

Individual cycle images for the fueling sweep are available in Figure 5.25. For the richer fueling operating conditions, single cycle formaldehyde concentration is fairly uniform across the entire illuminated flow-field. The data for 5 mg exhibits the highest degree of inhomogeneity. It does not, however, show any preferential formation of formaldehyde in relationship to distance away from the window. Models predict that in cooler combustion environments caused by leaner equivalence ratios, the boundary layer effect would be most prominent. It is expected that at this crank angle position, formaldehyde would show a weaker concentration near the wall compared with the bulk gas burning at a higher temperature. These images for the 2 and 5 mg per cycle operation do not indicate preferential formation at all. In fact, each of the sample single cycle images for the lowest equivalence ratio operating conditions indicates significant formaldehyde concentration at the window surface.

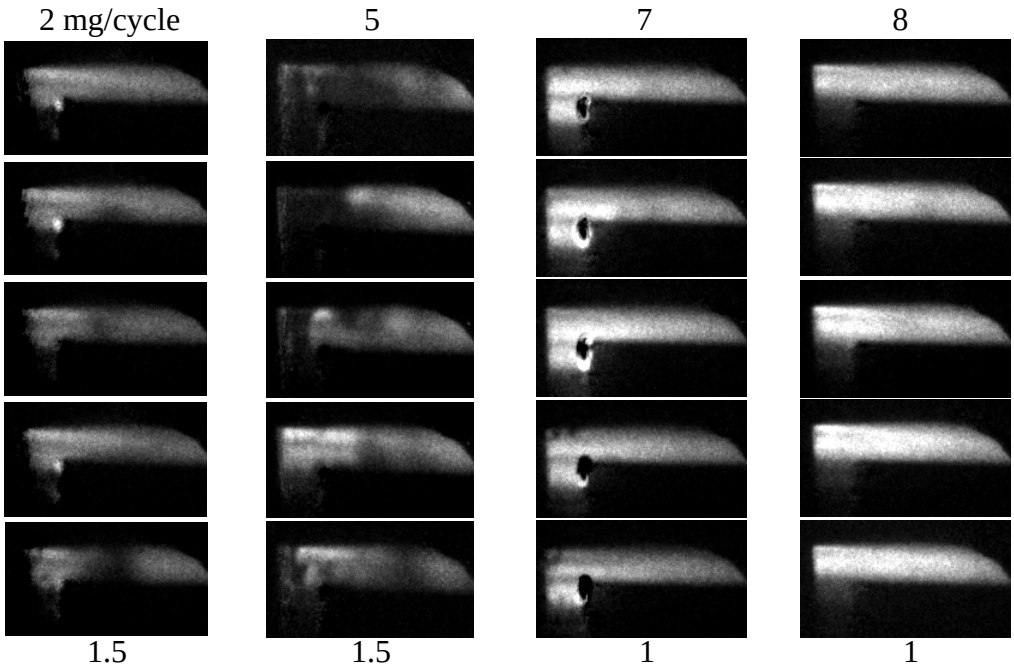

Figure 5.25 Random images from each image fueling (indicated top). Image intensity is scaled to show detail (relative scale indicated bottom).

Figure 5.26 is a plot of intensity profiles for the averaged corrected data image with a 2 mg fueling rate and two samples of individual cycle corrected images. These line profiles show that contrary to the observed trend in the averaged profile for these light load images, formaldehyde does form with significant concentration near the inner window surface as in the richer cases.

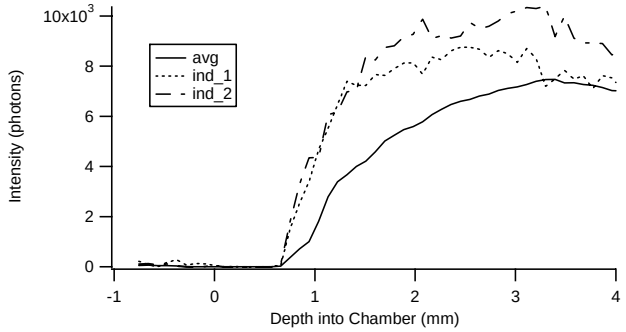

Figure 5.26 Intensity profile for average corrected fired image and two individual cycle images for 2 mg/cycle fueling, acquired at 10° bTDC.

6. Summary and Conclusions

6.1. Project Summary

The goal of this project was the visualization of formaldehyde in an HCCI engine in order to measure combustion quality near the chamber surfaces as an indicator of boundary layer effects. These images would, hopefully, provide information about the significance of the effect that thermal stratification near the chamber surfaces has on combustion quality and completeness. Experimental temperature measurements have shown high thermal gradients at the chamber walls, suggesting a very thin boundary layer. Chemical kinetics and CFD computer modeling have suggested a much thicker boundary layer effect.

The visualization was accomplished with the use of an imaging technique known as Planar Laser-Induced Fluorescence (PLIF) and a high resolution intensified charge-coupled device (ICCD) camera, both accessing the combustion chamber through a window in the clearance volume. Formaldehyde was excited with 355 nm light from a pulsed Nd:YAG laser that propagated across the camera's field of view and into the combustion chamber. Images were corrected through averaging and background subtraction.

6.2. Conclusions

Based on the image data analyzed in this thesis, the main conclusion that can be drawn from the work is the absence of a strong global thermal stratification effect on the reacting fluid near the combustion chamber wall. All operating conditions show formaldehyde in significant concentrations near the chamber walls indicating relatively

homogeneous combustion and a small thermal boundary layer. Measurements of the maximum spatial resolution of the camera indicate that the data images are resolved at the inner window surface to that limit. Model predictions, such as those in [12] and [26], of a large boundary layer effect in the form of reduced formaldehyde formation near the wall during the first stage combustion and persisting formaldehyde concentrations near the wall after the second stage of combustion, are not supported by the data.

Trends in formaldehyde concentration as a function of crank angle and equivalence ratio were consistent with literature reports such as [25]. Timing sweep data showed formaldehyde formation during the first stage of combustion and consumption during the second for equivalence ratios rich enough to exhibit two-stage combustion. Individual cycle images indicated that formaldehyde structure in the combustion chamber early and late in the combustion cycle is heterogeneous. There is no indication of preferential formation or consumption locations. For the data associated with the fueling sweep, the fluorescence signal was seen to increase with an increase in equivalence ratio. Leaner operating conditions showed that, with the lack of a main heat release, formaldehyde persisted and was recorded as late in the cycle as 20° aTDC.

6.3. Recommendations for Future Work

Results obtained in this project are mostly qualitative and relative due to the absence of a scaling relationship between image intensity and formaldehyde number density. Seeding of the intake stream with formaldehyde in aqueous solution was attempted in an effort to develop this relationship. A known concentration of formaldehyde was drawn through the combustion chamber for fluorescence in a motoring engine. Unfortunately, no signal was

captured in the recoded images. The reason for this failure was not determined. Formaldehyde seeding was previously performed in [25], but with a high level of uncertainty with concentration due to the extremely low flow rate used to simulate typical in-cylinder formaldehyde concentrations. Therefore, work to develop a scaled relationship through flatfield normalizing would benefit the analysis by providing a more quantitative view.

Laser power drift also occurs over extended periods of firing and must be considered when evaluating image intensity. During data collection the laser power was observed to fall gradually over time. Since the fluorescence signal intensity is related to laser power, a significant difference in laser power from one data set to the next could skew relative concentration estimations. Multiple times during data collection, the laser power was adjusted to maintain a constant output level. Normalization by laser power could also be accomplished with flatfield images taken periodically during data acquisition.

Bibliography

[1] Stanglmaier, R.H. and Roberts, C.E., 1999, “Homogeneous Charge Compression Ignition (HCCI): Benefits, Compromises, and Future Engine Applications,” SAE 1999-01-3682.

[2] Najt, P.M. and Foster, D.E., 1983, “Compression-Ignited Homogeneous Charge Combustion,” SAE 830264.

[3] Sanders, S.T., Kim, T., and Ghandhi, J.B., 2003, “Gas Temperature Measurements During Ignition in an HCCI Engine,” SAE 2003-01-0744.

[4] Christensen, M. and Johansson, B., 1999, “Homogeneous Charge Compression Ignition with Water Injection,” SAE 1999-01-0182.

[5] Peng, Z., Zhao, H., and Ladommatos, N., 2003, “Effects of Air/Fuel Ratios and EGR Rates on HCCI Combustion of n-heptane, a Diesel Type Fuel,” SAE 2003-01-0747.

[6] Christensen, M., Johansson, B., Amneus, P., and Mauss, F., 1998, “Supercharged Homogeneous Charge Compression Ignition,” SAE 980787.

[7] Christensen, M., Johansson, B., 1998, “Influence of Mixture Quality on Homogeneous Charge Compression Ignition,” SAE 982454.

[8] Heywood, J., 1988, *Internal Combustion Engine Fundamentals*, McGraw-Hill, New York.

[9] Flynn, P.F., Hunter, G.L., Durrett, R.P., Farrell, L.A., and Akinyemi, W.C., 2000, “Minimum Engine Flame Temperature Impacts on Diesel and Spark-Ignition Engine NOx Production,” SAE 2000-01-1177.

[10] Aroonsrisopon, T., Foster, D., Morikawa, T., and Iida, M., 2002, “Comparison of HCCI Operating Ranges for Combinations of Intake Temperature, Engine Speed and Fuel Composition,” SAE 2002-01-1924.

[11] Epping, K., Aceves, S., Bechtold, R., and Dec, J., 2002, “The Potential of HCCI Combustion for High Efficiency and Low Emissions,” SAE 2002-01-1923.

[12] Aceves, S.M., Flowers, D.L., Westbrook, C.K., Smith, J.R., Pitz, W., Dibble, R., Christensen, M., Johansson, B., 2000, “A Multi-Zone Model for Prediction of HCCI Combustion and Emissions,” SAE 2000-01-0327.

[13] Lee, T., Bessler, W.G., Schulz, C., Patel, M., Jefferies, J.B., Hanson, R.K., 2004, "UV planar laser induced fluorescence imaging of hot carbon dioxide in a high-pressure flame," *Applied Physics B (Lasers and Optics)*, v.79, pp.427-430.

[14] Bright, A.G., 2004, *Residual Gas Mixing in Engines*, M.S. Thesis, Department of Mechanical Engineering, University of Wisconsin-Madison.

[15] Wiles, M.A., 2003, *Characterization of Operating Parameters' Authority on the Flow-Field Mixedness of a DISI Engine*, M.S. Thesis, Department of Mechanical Engineering, University of Wisconsin-Madison.

[16] Hanson, R.K., Seitzman, J.M., Paul, P.H., 1990, "Planar Laser-Fluorescence Imaging of Combustion Gases," *Applied Physics B (Lasers and Optics)*, v. 50, pp.441-454.

[17] Rothamer, D.A., Ghandhi, J.B., 2002, "On the Calibration of Single-Shot Planar Laser Imaging Techniques in Engines," SAE 2002-01-0748.

[18] Collin, R., Nygren, J., Richter, M., Alden, M., Hildingsson, L., and Johansson, B., 2003, "Simultaneous OH-and Formaldehyde-LIF Measurements in an HCCI Engine," SAE 2003-01-3218.

[19] Hultqvist, A., Engdar, U., Johansson, B., and Klingmann, J., 2001, "Reacting Boundary Layers in a Homogeneous Charge Compression Ignition (HCCI) Engine," SAE 2001-01-1032.

[20] Ozisik, M.N., 1985, *Heat Transfer: A Basic Approach*, McGraw-Hill, Boston, MA.

[21] Fiveland, S.B. and Assanis, D.N., 2001, "Development of a Two-Zone HCCI Combustion Model Accounting for Boundary Layer Effects," SAE 2001-01-1028.

[22] Lyford-Pike, E.J. and Heywood, J.B., 1984, "Thermal boundary layer thickness in the cylinder of a spark-ignition engine," *International Journal of Heat and Mass Transfer*, v.27, no.10, pp.1873-1878.

[23] Yu, W., 2004, "Practical Anti-vignetting Methods for Digital Cameras," *IEEE Transactions on Consumer Electronics*, v.50, no.4, pp.975-983.

[24] Yamada, T., Tsubouchi, K., "Development of small pixel and high performance CCD image sensors," *Record of Electrical and Communication Engineering Conversazione Tohoku University*, v.71, n.2, pp.57-60.

[25] Kim, T. and Ghandhi, J.B., 2005, "Investigation of Light Load HCCI Combustion using Formaldehyde Planar Laser-Induced Fluorescence," Combustion Institute 30.

[26] Aceves, S.M., Flowers, D.L., Espinosa-Loza, F., Martinez-Frias, J., Dec, J.E., Sjoberg, M., Dibble, R.W., Hessel, R.P., 2004, "Spatial Analysis of Emissions Sources for HCCI Combustion at Low Loads Using a Multi-Zone Model," SAE 2004-01-1910.

[27] Brackmann, C., Bood, J., Afzelius, M., and Bengtsson, P-E., 2004, "Thermometry in internal combustion engines via dual-broadband rotational coherent anti-Stokes Raman spectroscopy," *Institute of Physics: Measurement Science and Technology*, v.15, no.3, pp.13-25.

[28] Iverson, R.J., 2004, *The Effect of Intake Charge Stratification on HCCI Combustion*, M.S. Thesis, Department of Mechanical Engineering, University of Wisconsin-Madison.

[29] van Walree, P., "Optics page," Van Walree photography & optics, Paul van Walree, 14 May 2005, 18 August 2005, <http://www.vanwalree.com/optics/vignetting.html>.

[30] Bes Optics Inc., 18 August 2005, <http://www.besoptics.com>.

[31] Andover Corporation, 18 August 2005, <http://www.andcorp.com>.

Appendix A – Piston Ring Details

Description	Part Number
Vespel butt-cut compression ring	571696MFM
Bronze-impregnated Nylon upper rider ring	571697MFB
Bronze-impregnated Nylon upper rider ring	571697MFB
Bronze-impregnated Nylon lower rider ring	571698MFB
Oil control ring	571694KGG

Appendix B – Engine Component Drawings

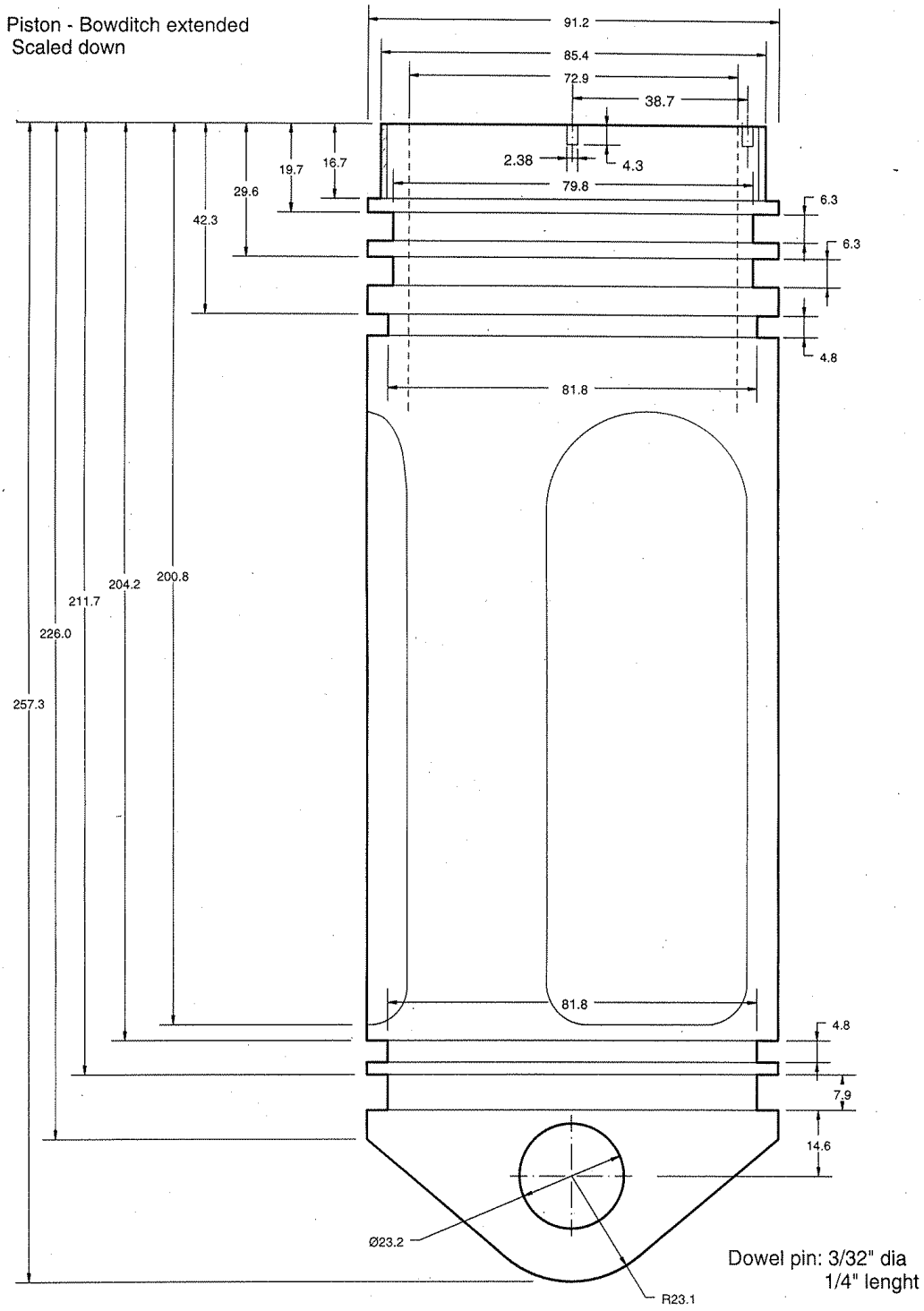

CYLINDER HEAD - Bottom View

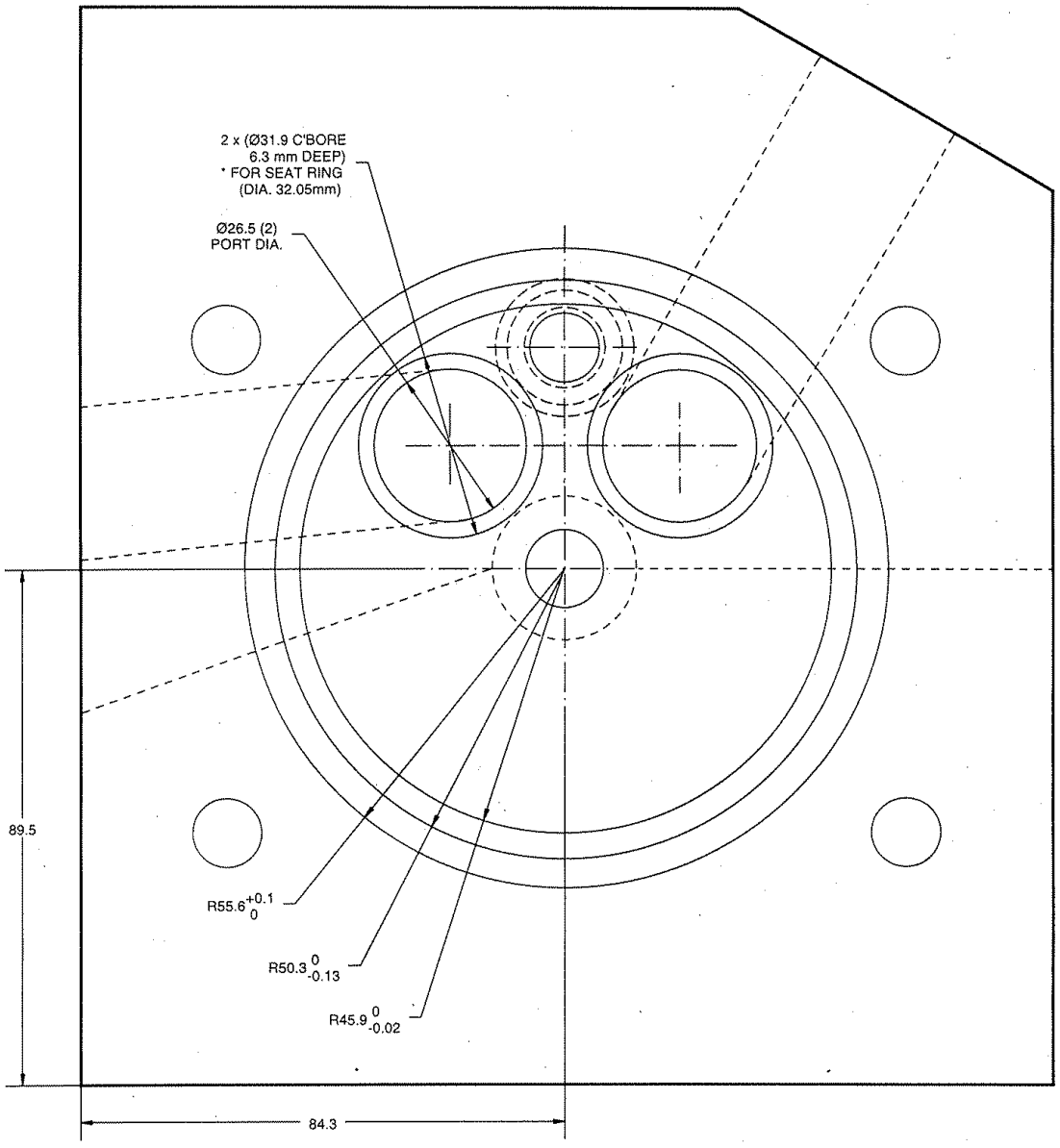

Notes:
1. Some hidden lines removed
2. Groove designed for O-ring AS-568A-243

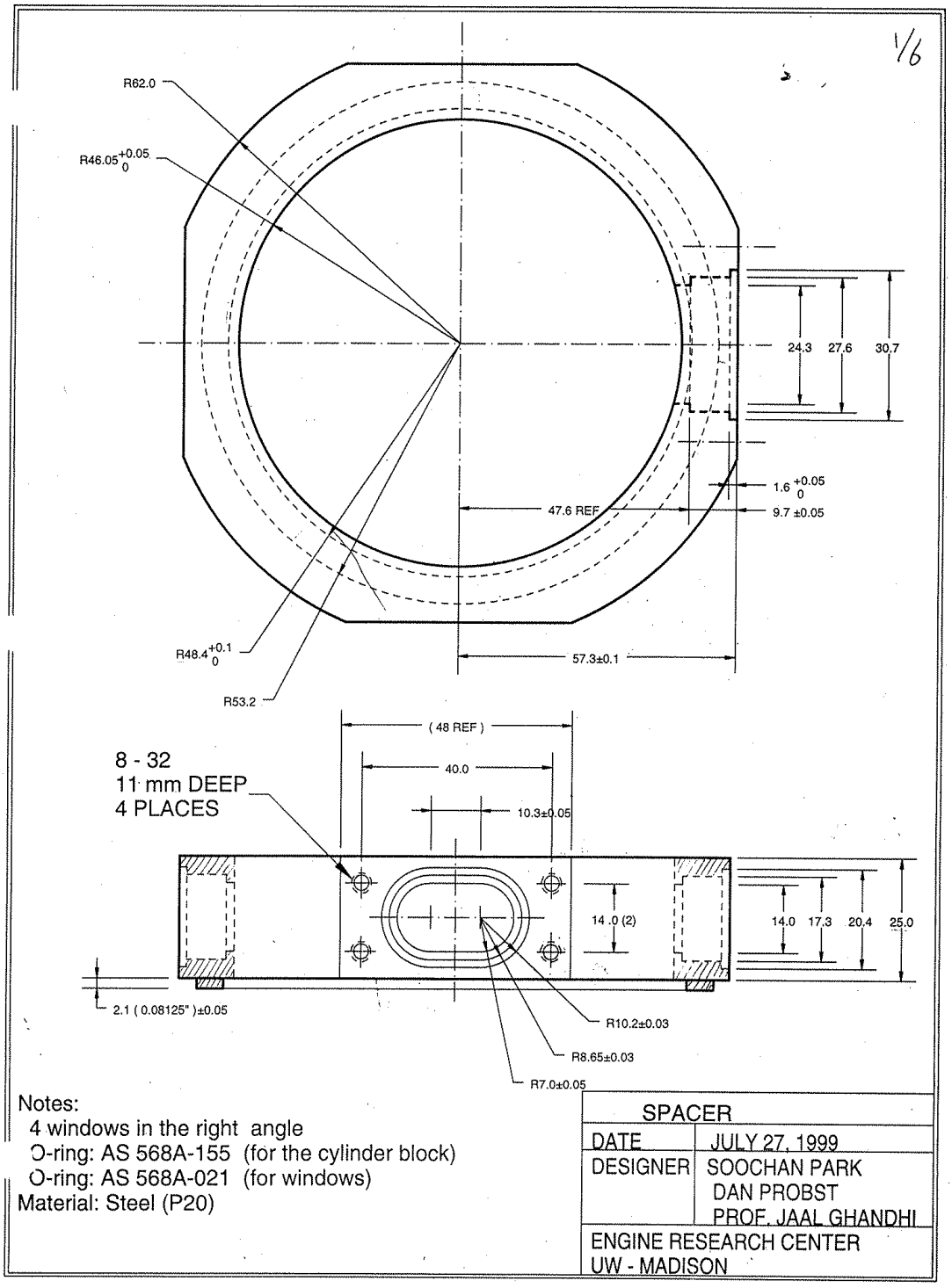

Notes:
4 windows in the right angle
O-ring: AS 568A-155 (for the cylinder block)
O-ring: AS 568A-021 (for windows)
Material: Steel (P20)

SPACER	
DATE	JULY 27, 1999
DESIGNER	SOOCHAN PARK DAN PROBST PROF. JAAL GHANDHI
ENGINE RESEARCH CENTER UW - MADISON	

3/6

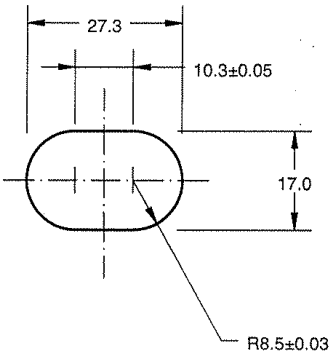

Thickness = 16.5

MATERIAL: P20
QUANTITY: 4
UNIT: mm

CAP - WINDOW	
DATE	JULY 27, 1999
DESIGNER	SOOCHAN PARK DAN PROBST PROF. JAAL GHANDHI
ENGINE RESEARCH CENTER UW - MADISON	

2/6

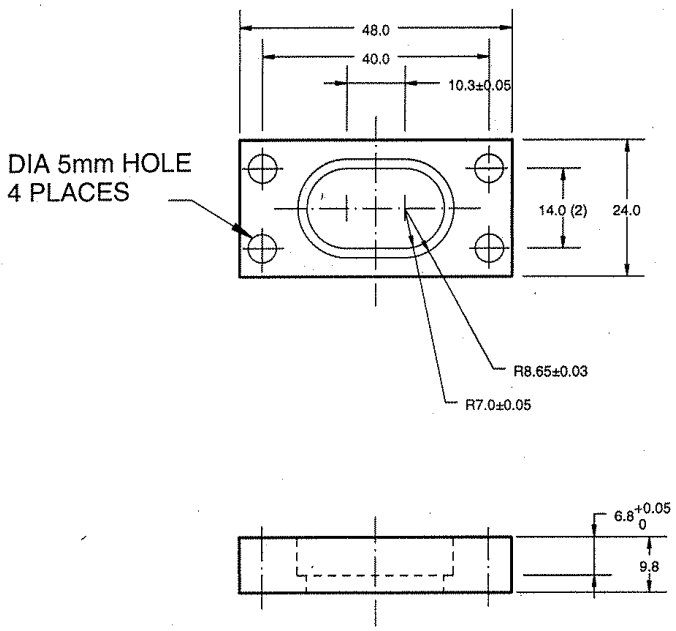

Material: Steel (P20)
Quantity: 4

PLATE - CLAMPING	
DATE	JULY 27, 1999
DESIGNER	SOOCHAN PARK DAN PROBST PROF. JAAL GHANDHI
ENGINE RESEARCH CENTER UW - MADISON	

Appendix C – Valve Events

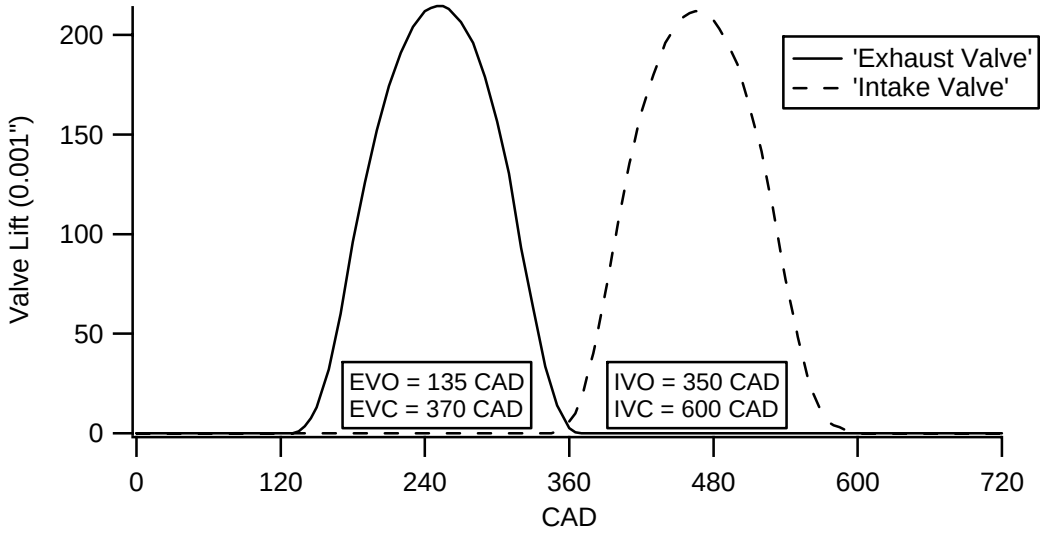

Appendix D – Intake Orifice Flow Calibrations

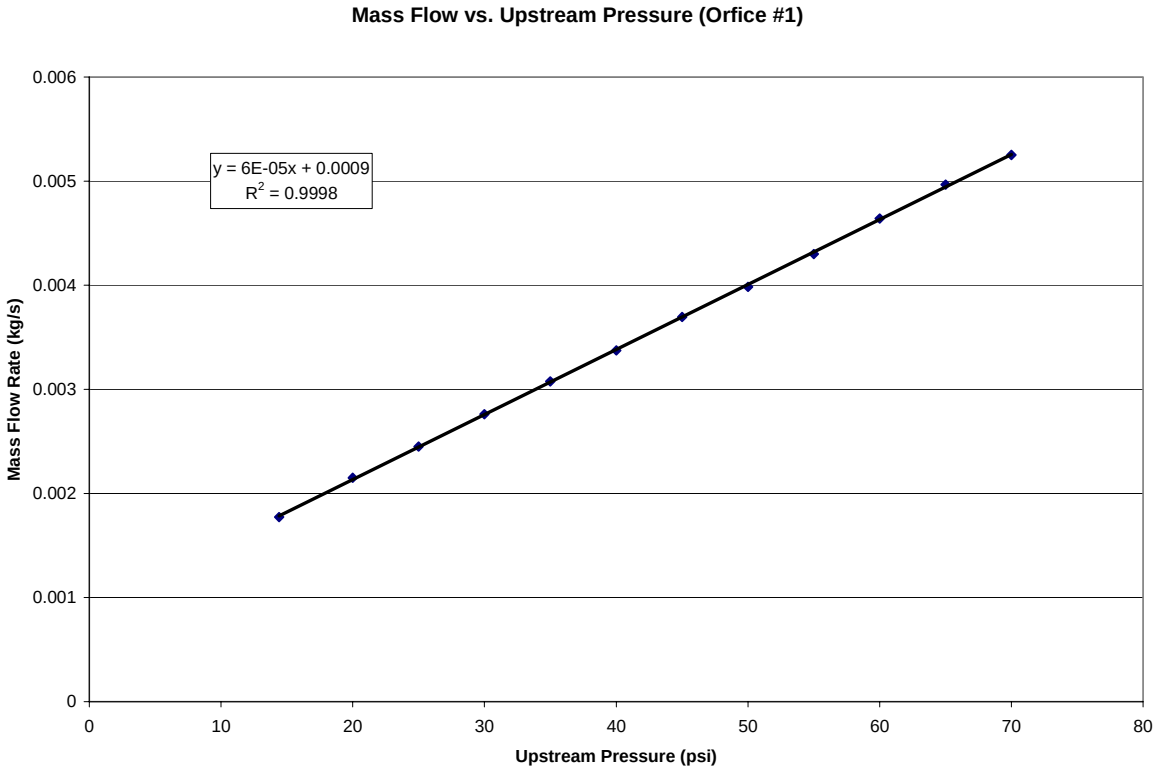

Appendix E – Fuel Injector Flow Calibrations

RPM	Fuel Input	Fuel Out	Time	IPS	# of Inj	Flow Rate	Fuel Output
(rev/min)	*(mg/inj)*	*(cc)*	*(s)*	*(inj/sec)*	*(inj)*	*(cc/inj)*	*(mg/inj)*
600	2	9	299.91	5	1499.55	0.006001801	4.102830849
600	4	14	299.81	5	1499.05	0.009339248	6.384310063
600	6	19	299.91	5	1499.55	0.012670468	8.661531793
600	8	23	299.78	5	1498.9	0.015344586	10.48955901
600	10	28	299.84	5	1499.2	0.018676628	12.76734258
600	12	32	299.9	5	1499.5	0.021340447	14.58832944
600	14	36	299.85	5	1499.25	0.024012006	16.4146073
600	16	39.5	299.87	5	1499.35	0.026344749	18.00927068
600	18	43.25	299.97	5	1499.85	0.028836217	19.71243791
600	20	49	299.87	5	1499.35	0.032680828	22.34061427

**** fuel density = 683.6 mg/cc**

Appendix F – Pressure Transducer Calibration